Hindawi
Journal of Applied Mathematics
Volume 2024, Article ID 9993489, 16 pages
https://doi.org/10.1155/2024/9993489

Research Article

Performance Analysis of Thermal and Surface Roughness Effect of Slider Bearings with Unsteady Fluid Film Lubricant Using Finite Element Method

Girma Desu Tessema, Getachew Adamu Derese, and Awoke Andargie Tiruneh

Department of Mathematics, College of Sciences, Bahir Dar University, Bahir Dar, Ethiopia

Correspondence should be addressed to Girma Desu Tessema; girmadesu11@gmail.com

Received 23 June 2023; Revised 12 October 2023; Accepted 14 November 2023; Published 16 January 2024

Academic Editor: Qiankun Song

The streamline upwind Petrov-Galerkin (SUPG) finite element method was used in this study to investigate the thermal and surface roughness effects on an inclined slider bearing with an unsteady fluid film. One-dimensional transverse and longitudinal surface roughness models were considered with the supposition that roughness is stochastic and has a Gaussian random distribution. For simplicity of numerical computation, the irregularity caused by the texture of the surface is transformed into a regular domain. The bearing performance of the combined effect is lower than the thermal and surface roughness effects of the one-dimensional longitudinal surface roughness for all modified Reynolds numbers of nonparallel slider bearings; this means that for nonparallel ($w = 0.4$) between the surface roughness effect and the combined effect condition, there is a decrease of 13% in load-carrying capacity performance and a minimal change in friction force, respectively. However, in the case of nonparallel one-dimensional transverse type slider bearings, the bearing performance of the thermal effect is lower than the combined and surface roughness effects for all modified Reynolds numbers, where between the combined effect and the thermal effect condition, there is a reduction of 19% in load-carrying capacity performance and 2% in friction force practically for all changed Reynolds values, respectively. Furthermore, the combined effects at various temperatures have been investigated. As a result, in both longitudinal and transverse models, in the case of the pad temperature being lower than the slider, the load-carrying capacity performance is higher than in other cases for nonparallel slider bearings, whereas when the slider temperature is lower than the pad temperature, the drag frictional force is the leading one in both models. In general, considering surface texture and inertial effects will increase the performance of a slider. The results obtained are displayed using figures and tables.

1. Introduction

Slider bearings are a type of bearing in which one surface can move over another. They are frequently employed in industrial, agricultural, and automotive applications. Slider bearings can operate at extremely high speeds and can support heavy weights. They are a great option for applications that demand long-term dependability because of their resistance to wear and tear. The geometry of a rough slider bearing is important in many applications, from engineering to the automotive industry. Additionally, the geometry affects the load capacity of the bearing as well as its wear characteristics. Thus, properly understanding the geometry of the bearing is critical for any successful application.

Various bearing types with surface roughness effects have been examined by numerous researchers. Hydrostatic bearings were examined by Lin [1], journal bearings by Guha [2], and slider bearings by Christensen and Tonder [3]. For a nonisothermal flow with temperature-dependent density and viscosity in a high-speed slider bearing model, Kumar [4] examined a segregated FEM of the Petrov-Galerkin framework with appropriately SUPG weight

functions. Rathish Kumar and Srinivasa Rao [5] examined the use of the SUPG-FEM in the numerical modelling of slider bearings to determine load-carrying support.

Andharia et al. [6] examined how surface roughness affected hydrodynamic slider bearing performance. The bearing surface topography is assumed to be characterized by a stochastic random variable with nonzero mean, variance, and skewness, which is a generalized version of surface roughness. Film shapes such as secant, flat, exponential, and hyperbolic sliders are studied. Alyaqout and Elsharkawy [7] enhance the slider bearing geometry using a thermohydrodynamic bearing model. Thakkar et al. [8] used a stochastic model to account for the impact of surface roughness while examining the behavior of transversely rough narrow-width tapered pad bearings.

A theoretical model was created by Chawla and Bhardwaj [9] to study how couple stress on fluid-lubricated surfaces is affected by surface roughness. Rahman [10] reports that an external transverse magnetic field has been obtained and numerically studied to investigate the effects of unsteady flow and heat transfer in an incompressible laminar, electrically conducting, and non-Newtonian fluid over a nonisothermal stretching sheet with variation in viscosity and thermal conductivity in a porous medium. The unsteady flow of a non-Newtonian fluid over an oscillating vertical porous plate in the presence of a uniform magnetic field has been studied by Ali et al. [11]. Using an accurate computer model of the complete set of the Navier-Stokes equations for incompressible flows, the influence of inertial forces in stable and unsteady lubrication films was investigated Sestieri and Piva [12].

The numerical analysis of the time-dependent magnetized micropolar fluid flow over a curved surface was examined by Abbas et al. [13]. The impacts of thermal jumped and velocity slip are taken into consideration on the curved surface.

Many scholars have investigated inertial effects, such as Syed and Sarangi [14] on hydrodynamic lubrication with deterministic micro textures, taking the fluid inertia effect into account. Although the Reynolds equation is widely used in thin film lubrication, its application to textured surfaces is not entirely convincing, particularly at moderate to high Reynolds numbers. They have obtained that fluid inertia, which is generally neglected in the Reynolds equation but becomes significant. A perturbation analysis was performed by Ota et al. [15] on a modified Reynolds equation to study the effect of inertia on film rupture in hydrodynamic lubrication. Malvano and Vatta [16] studied the influence of fluid inertia flow on steady laminar lubrication. Prasad et al. [17] examined a theoretical aspect of the hydrodynamic lubrication of two symmetric rollers by power-law fluids.

The thermohydrodynamic analysis of plane slider bearing with roughness was analyzed by Sinha and Adamu [18] using the finite difference method, where surface roughness is assumed to be stochastic and Gaussian randomly distributed. Adamu and Sinha [19] also considered heat conduction through both the pad and slider by taking into account two models of one-dimensional longitudinal and transverse roughness. Singh et al. [20] reported a numerical study of the hydrodynamic lubrication of slider bearings with textured surfaces. Extreme industrial conditions necessitate the use of a bearing that can withstand high-speed operations, heavy loads, and high stiffness, among other things. Alexander Raymand and Jayakaran Amalraj [21] considered the combined effects of fluid inertia forces and non-Newtonian characteristics with the Herschel-Bulkley fluid as a lubricant in an externally pressurized converging thrust bearing.

Recently, Desu Tessema et al. [22] and Tessema et al. [23] using the streamline upwind Petrov-Galerkin (SUPG) finite element method (FEM) examined the performance of slider bearings with the effects of thermal and surface roughness on one-dimensional longitudinal and transverse roughness types under laminar and turbulent conditions. Naduvinamani and Angadi [24] examined the static and dynamic properties of a few stress fluid-lubricated rough, porous Rayleigh step bearings. Naduvinamani and Angadi [25] analyzed the effects of micropolar fluid and roughness on inclined porous slider bearings' dynamic characteristics. Theoretical and numerical analyses were used to investigate the static properties of aerostatic porous journal bearings by Gu et al. [26]. Fang et al. [27] discussed transient elastohydrodynamic lubrication under line contact stiffness and damping behaviors. Jamshed et al. [28] used a single-phase optimized entropy analysis to illustrate the thermal efficiency improvement of solar aircraft employing unsteady hybrid nanofluids. Raees et al. [29] examined the transfer of energy in the power-law nanofluid driven to flow along a horizontal wall by magnetization. Overall, our examination of the literature and our knowledge gaps show that SUPG-FEM has not been used to address the performance of slider bearings when surface roughness and coupled heat effects are present along with an unsteady fluid film that takes into account various inertial effects.

Nonetheless, our noteworthy input to this study consists of developing the governing Reynolds equation (found in equations (12) and (15)) for surface roughness (for one-dimensional longitudinal and transverse) with thermal impact for slider bearing. The combined effect of temperature and surface roughness on tilted pad slider bearings with the unsteady fluid flow by SUPG-FEM has received little attention. Thus, the combined effect of temperature and surface roughness on a slider bearing with an unsteady fluid film, considering the inertial effect, will be numerically analyzed in this study using SUPG-FEM.

2. Governing Equations

Figure 1 hereunder illustrates the geometry of a rough slider bearing. Comparing the length of the bearing in the direction orthogonal to the xy-plane to the height of the fluid film thickness h, a fairly long length is assumed.

The simplified equations for the flow of lubricants in slider bearings are derived from the governing equations of fluid flow. These equations took into account the viscosity and density of the lubricant and the speed of the bearing, as well as other variables such as the bearing geometry, the applied load, and the temperature of the lubricant.

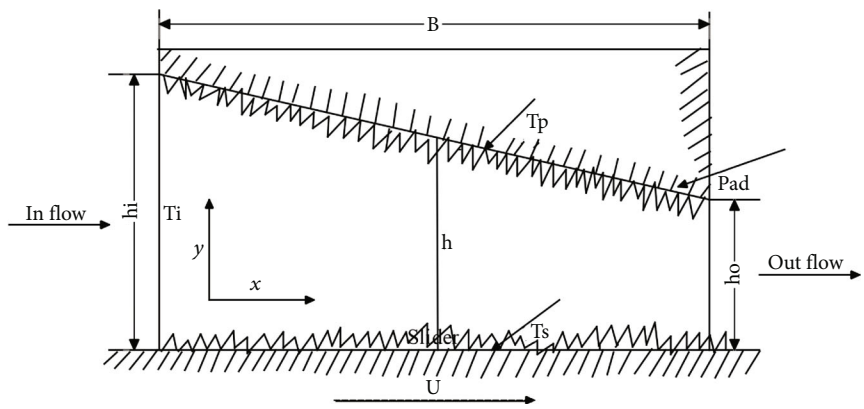

Figure 1: Geometry of one-dimensional transverse roughness of slider bearing.

The modified Reynolds lubrication equation was developed using the averaged inertia method as given in Hooke [30]. This is the most common method for obtaining the extended form of the Reynolds equation, which includes fluid inertia effects. The initial system of equations is replaced with an approximate system of equations obtained by averaging the inertial terms across the fluid film thickness. To derive the governing equation, the following assumptions are considered: the fluid is Newtonian lubricant; the fluid film thickness is significantly less than other bearing dimensions; in fluid flow, the inertial effect is considered; body force is negligible; the flow is laminar; and there is no slip at the bearing surfaces.

Following the above assumptions, the following equations are obtained:

Momentum equation:

$$\frac{\partial(\rho u)}{\partial t} + u\frac{\partial(\rho u)}{\partial x} + v\frac{\partial(\rho u)}{\partial y} = -\frac{dp}{dx} + \frac{\partial}{\partial y}\left(\mu\frac{\partial u}{\partial y}\right). \quad (1)$$

Continuity equation:

$$\frac{\partial}{\partial x}(\rho u) + \frac{\partial}{\partial y}(\rho v) = 0. \quad (2)$$

Eqs. (1) and (2) are combined to generate the general Reynolds equation for unsteady fluid flow lubricant by applying the boundary conditions $u = U$ and $v = 0$ on the moveable slider, $u = v = 0$ on the stationary pad, and substituting ρ by ρ_{av} and μ by μ_{av}, respectively.

The generalized equation of Reynolds has a form of

$$\frac{\partial}{\partial x}\left(\frac{\rho_{\text{av}}H_t^3}{\mu_{\text{av}}}\frac{dp}{dx}\right) = 6U\frac{\partial}{\partial x}(\rho_{\text{av}}H_t) + \frac{\rho_{\text{av}}H_t^2}{\mu_{\text{av}}} \cdot \left(U\frac{\partial^2(\rho_{\text{av}}H_t)}{\partial x\partial t} + U\frac{\partial^2(\rho_{\text{av}}H_tU_m)}{\partial x^2} - \frac{\partial^2(\rho_{\text{av}}H_tU_m)}{\partial x\partial t} - \frac{\partial^2(\rho_{\text{av}}H_tU_m^2)}{\partial x^2}\right), \quad (3)$$

where

$$U_m = \frac{1}{h}\int_0^h u dy \quad (4)$$

is the mean velocity and H_t is the lubricant film thickness. Along with the lubricating presumption mentioned above, the following were taken into account for the equation of energy:

(1) Conduction terms other than those across the fluid film are negligible

(2) Constant-specific heat and thermal conductivity are assumed

The equation of energy becomes as follows:

$$\rho c\left(u\frac{\partial T}{\partial x} + v\frac{\partial T}{\partial y}\right) = k\frac{\partial^2 T}{\partial y^2} + \mu\left(\frac{\partial u}{\partial y}\right)^2 + u\frac{\partial p}{\partial x}. \quad (5)$$

The following equations indicate temperature-dependent density and viscosity:

$$\begin{aligned}\rho &= \rho_0(1 - \lambda(T - T_a)),\\ \rho_{\text{av}} &= \rho_a(1 - \lambda(T_{\text{av}} - T_a)),\end{aligned} \quad (6)$$

where λ is thermal expansion coefficient and ρ and ρ_a are the density at temperature T and ambient temperature T_a correspondingly.

$$\begin{aligned}\mu &= \mu_0 \exp\left[-\beta(T - T_a)\right],\\ \mu_{\text{av}} &= \mu_a \exp\left[-\beta(T_{\text{av}} - T_a)\right],\end{aligned} \quad (7)$$

where μ_a and μ are the viscosities at temperature T_a and T, respectively, at ambient pressure and β is the temperature-viscosity coefficient.

An isothermal HD lubrication of rough surface bearings of stochastic theory with rapidly varying quantity developed by Christensen and Tonder [31] and Christensen [32], a Reynolds type equation in the average pressure to rough

surface bearings was formulated by taking the film thickness as a stochastic process.

The thickness of the lubricant film considered in this work on the slider bearing has a geometry of two parts:

$$H_t(x, z, \epsilon) = h_0(x) + \delta(x, z, \epsilon), \tag{8}$$

where h_0 is the nominal (smooth) part, which measures the large-scale part of the film geometry, including any long wavelength disturbances, and δ is a randomly varying quantity with a zero mean, which arises due to the surface roughness measured from the nominal level. In order to deal with a one-dimensional rough surface, this paper uses the following two additional assumptions introduced by Christensen and Tonder [31] and Christensen [32] in order to establish a foundation for the use of stochastic theory:

(i) The variance of the pressure gradient of unsteady fluid flow film in the roughness direction is negligible

(ii) The variance of unit flow of unsteady fluid flow film is negligible in the direction perpendicular to the roughness. In this analysis, the assumptions of Christensen and Tonder [31] and Christensen [32] will be extended to the HD lubrication of rough surface bearings with temperature-dependent ρ and μ by imposing the following extra assumption for velocity and temperature variables due to Sinha and Adamu [18]. Temperature, velocity, and U_m magnitudes associated with roughness are negligible in comparison to the corresponding general magnitudes in the bearing. As a result, the variances of ρ, μ, temperature gradients $\partial T/\partial y$, and velocity gradients $\partial u/\partial y$ in the direction of roughness are negligible

According to assumption (ii), the magnitude of the average temperature T_{av} and U_m associated with roughness is negligible. As a result, the magnitudes of ρ_{av} and μ_{av} associated with roughness are small. The theory is applied to longitudinal and transverse roughness patterns. In the longitudinal roughness model, roughness is assumed to take the form of long, narrow furrows and ridges in the sliding surface (x-direction). As a result, the film thickness can be described as a function of the form.

$$H_t(x, z, \epsilon) = h(x) + \delta(z, \epsilon). \tag{9}$$

Similarly, the roughness in the transverse roughness model is assumed to take the form of long, narrow ridges and furrows running perpendicular to the sliding direction.

Hence, the film thickness becomes part of the form:

$$H_t(x, z, \epsilon) = h(x) + \delta(x, \epsilon). \tag{10}$$

Taking the expected values on both sides of the Reynolds equation for unsteady fluid flow film given in Eq. (3), $E(h_s)$ is the expectancy operator defined by

$$E(h_s) = \int_{-\infty}^{\infty} h_s f(h_s) dh_s, \tag{11}$$

and $f(h_s)$ is the probability density distribution for the stochastic variable h_s.

Using the aforementioned assumptions (i) and (ii), as well as some of the details given in Sinha and Adamu [18], the modified Reynolds equation for unsteady fluid flow film of longitudinal roughness is as follows:

$$\begin{aligned}\frac{\partial}{\partial x}\left(\frac{\bar{\rho}_{\text{av}}\left(h^3 + 3h\sigma^2\right)}{\bar{\mu}_{\text{av}}}\frac{d\bar{p}}{dx}\right) &= 6U\frac{\partial}{\partial x}\left(\bar{\rho}_{\text{av}}h\right) + \frac{\bar{\rho}_{\text{av}}\left(h^2 + \sigma^2\right)}{\bar{\mu}_{\text{av}}} \\ &\cdot\left(U\frac{\partial^2\left(\bar{\rho}_{\text{av}}h\right)}{\partial x\partial t} + U\frac{\partial^2\left(\bar{\rho}_{\text{av}}h\bar{U}_m\right)}{\partial x^2}\right. \\ &\left. - \frac{\partial^2\left(\bar{\rho}_{\text{av}}h\bar{U}_m\right)}{\partial x\partial t} - \frac{\partial^2\left(\bar{\rho}_{\text{av}}h\bar{U}_m^2\right)}{\partial x^2}\right).\end{aligned} \tag{12}$$

Following assumption (ii), approximations of u and $\partial(\rho u)/\partial x$, v and $\partial(\rho u)/\partial y$, μ and $\partial u/\partial y$, ρ and u, and ρ and v are independent random variables, and taking expected values in both sides of Eq. (1) and Eq. (2), we can get

$$\begin{aligned}\frac{\partial(\bar{\rho}\bar{u})}{\partial t} + \bar{u}\frac{\partial(\bar{\rho}\bar{u})}{\partial x} + \bar{v}\frac{\partial(\bar{\rho}\bar{u})}{\partial y} &= -\frac{d\bar{p}}{dx} + \frac{\partial}{\partial y}\left(\bar{\mu}\frac{\partial\bar{u}}{\partial y}\right), \\ \frac{\partial}{\partial x}(\bar{\rho}\bar{u}) + \frac{\partial}{\partial y}(\bar{\rho}\bar{v}) &= 0.\end{aligned} \tag{13}$$

Taking assumptions (i) and (iii) into account, the transformed energy equation will be

$$\bar{\rho}c\left(\bar{u}\frac{\partial\bar{T}}{\partial x} + \bar{v}\frac{\partial\bar{T}}{\partial y}\right) = k\frac{\partial^2\bar{T}}{\partial y^2} + \bar{\mu}\left(\frac{\partial\bar{u}}{\partial y}\right)^2 + \bar{u}\frac{\partial\bar{p}}{\partial x}. \tag{14}$$

The transverse roughness modified Reynolds equation for unsteady fluid flow film becomes

$$\begin{aligned}\frac{\partial}{\partial x}\left(\frac{\bar{\rho}_{\text{av}}\left(h^3 - 6h\sigma^2\right)}{\bar{\mu}_{\text{av}}}\frac{d\bar{p}}{dx}\right) &= 6U\frac{\partial}{\partial x}\left[\bar{\rho}_{\text{av}}h\left(1 - \frac{3\sigma^2}{h^2}\right)\right] \\ &+ \frac{\bar{\rho}_{\text{av}}\left(h^2 + \sigma^2\right)}{\bar{\mu}_{\text{av}}}\left[U\frac{\partial^2\left(\bar{\rho}_{\text{av}}h\right)}{\partial x\partial t} + U\frac{\partial^2\left(\bar{\rho}_{\text{av}}\bar{U}_m h\right)}{\partial x^2}\right. \\ &\left. - \frac{\partial^2\left(\bar{\rho}_{\text{av}}\bar{U}_m h\right)}{\partial x\partial t} - \frac{\partial^2\left(\bar{\rho}_{\text{av}}\bar{U}_m^2 h\right)}{\partial x^2}\right].\end{aligned} \tag{15}$$

Transverse surface roughness, momentum, and continuity equations will take the same form as one-dimensional longitudinal surface roughness equations of unsteady fluid flow film.

The following nondimensional variable was used for this study:

$$\begin{aligned}
&u^{\circledast} = \frac{\bar{u}}{U}, U_m^{\circledast} = \frac{\bar{U}_m}{U}, v^{\circledast} = \frac{\bar{v}B}{Uh_i}, x^{\circledast} = \frac{x}{B}, y^{\circledast} = \frac{y}{h_i},\\
&t^{\circledast} = \frac{Ut}{B}, T^{\circledast} = \frac{\bar{T}}{T_a}, T_{\text{av}}^{\circledast} = \frac{\bar{T}_{\text{av}}}{T_a}, \mu^{\circledast} = \frac{\bar{\mu}}{\mu_a}, \mu_{\text{av}}^{\circledast} = \frac{\bar{\mu}_{\text{av}}}{\mu_a},\\
&\rho_{\text{av}}^{\circledast} = \frac{\bar{\rho}_{\text{av}}}{\rho_a}, \rho^{\circledast} = \frac{\bar{\rho}}{\rho_a}, p^{\circledast} = \frac{\bar{p}h_i^2}{\mu_a UB}, P_e = \frac{\rho_a Uch_i^2}{kB},\\
&\sigma^{\circledast} = \frac{\sigma}{h_i}, \bar{p}_i^{\circledast} = \frac{\bar{p}_i h_i^2}{\mu_a UB}, h^{\circledast} = \frac{h}{h_i}, \beta^{\circledast} = \beta T_a,\\
&\lambda^{\circledast} = \lambda T_a, P_r E_c = \frac{\mu_a U^2}{kT_a}, \delta^{\circledast} = \frac{\delta}{h_i}.
\end{aligned} \tag{16}$$

Equations (12), (13), (14), and (15) can be rewritten, respectively, as follows applying the above nondimensional variables:

$$\begin{aligned}
&\frac{\partial}{\partial x^{\circledast}}\left(\frac{\rho_{\text{av}}^{\circledast}\left(h^{\circledast 3} + 3h^{\circledast}\sigma^{\circledast 2}\right)}{\mu_{\text{av}}^{\circledast}}\frac{dp^{\circledast}}{dx^{\circledast}}\right)\\
&= 6\frac{\partial}{\partial x^{\circledast}}\left(\rho_{\text{av}}^{\circledast}h^{\circledast}\right) + \text{Re}^{\circledast}\left[\frac{\rho_{\text{av}}^{\circledast}\left(h^{\circledast 2} + \sigma^{\circledast 2}\right)}{\mu_{\text{av}}^{\circledast}}\right]\\
&\quad\cdot\left[\frac{\partial^2\left(\rho_{\text{av}}^{\circledast}h^{\circledast}\right)}{\partial x^{\circledast}\partial t^{\circledast}} + \frac{\partial^2\left(\rho_{\text{av}}^{\circledast}h^{\circledast}U_m^{\circledast}\right)}{\partial x^{\circledast 2}} - \frac{\partial^2\left(\rho_{\text{av}}^{\circledast}h^{\circledast}U_m^{\circledast}\right)}{\partial x^{\circledast}\partial t^{\circledast}} - \frac{\partial^2\left(\rho_{\text{av}}^{\circledast}h^{\circledast}U_m^{\circledast 2}\right)}{\partial x^{\circledast 2}}\right],
\end{aligned} \tag{17}$$

$$\begin{aligned}
&\frac{\partial}{\partial x^{\circledast}}\left(\frac{\rho_{\text{av}}^{\circledast}\left(h^{\circledast 3} - 6h^{\circledast}\sigma^{\circledast 2}\right)}{\mu_{\text{av}}^{\circledast}}\frac{dp^{\circledast}}{dx^{\circledast}}\right)\\
&= 6\frac{\partial}{\partial x^{\circledast}}\left[\rho_{\text{av}}^{\circledast}h^{\circledast}\left(1 - \frac{3\sigma^{\circledast 2}}{h^{\circledast 2}}\right)\right] + \text{Re}^{\circledast}\left[\frac{\rho_{\text{av}}^{\circledast}\left(h^{\circledast 2} + \sigma^{\circledast 2}\right)}{\mu_{\text{av}}^{\circledast}}\right]\\
&\quad\cdot\left[\frac{\partial^2\left(\rho_{\text{av}}^{\circledast}h^{\circledast}\right)}{\partial x^{\circledast}\partial t^{\circledast}} + \frac{\partial^2\left(\rho_{\text{av}}^{\circledast}U_m^{\circledast}h^{\circledast}\right)}{\partial x^{\circledast 2}} - \frac{\partial^2\left(\rho_{\text{av}}^{\circledast}U_m^{\circledast}h^{\circledast}\right)}{\partial x^{\circledast}\partial t^{\circledast}} - \frac{\partial^2\left(\rho_{\text{av}}^{\circledast}U_m^{\circledast 2}h^{\circledast}\right)}{\partial x^{\circledast 2}}\right],
\end{aligned} \tag{18}$$

$$\text{Re}^{\circledast}\left[\frac{\partial\left(\rho^{\circledast}u^{\circledast}\right)}{\partial t^{\circledast}} + u^{\circledast}\frac{\partial\left(\rho^{\circledast}u^{\circledast}\right)}{\partial x^{\circledast}} + v^{\circledast}\frac{\partial\left(\rho^{\circledast}u^{\circledast}\right)}{\partial y^{\circledast}}\right] = -\frac{dp^{\circledast}}{dx^{\circledast}} + \frac{\partial}{\partial y^{\circledast}}\left(\mu^{\circledast}\frac{\partial u^{\circledast}}{\partial y^{\circledast}}\right), \tag{19}$$

$$\frac{\partial}{\partial x^{\circledast}}\left(\rho^{\circledast}u^{\circledast}\right) + \frac{\partial}{\partial y^{\circledast}}\left(\rho^{\circledast}v^{\circledast}\right) = 0, \tag{20}$$

$$\rho^{\circledast}\left(u^{\circledast}\frac{\partial T^{\circledast}}{\partial x^{\circledast}} + v^{\circledast}\frac{\partial T^{\circledast}}{\partial y^{\circledast}}\right) = \frac{1}{P_e}\frac{\partial^2 T^{\circledast}}{\partial y^{\circledast 2}} + \frac{P_r E_c}{P_e}\mu^{\circledast}\left(\frac{\partial u^{\circledast}}{\partial y^{\circledast}}\right)^2 + \frac{P_r E_c}{P_e}u^{\circledast}\frac{dp^{\circledast}}{dx^{\circledast}}, \tag{21}$$

where

$$\text{Re}^{\circledast} = \left(\frac{\rho_a U h_i}{\mu_a}\right)\left(\frac{h_i}{B}\right) \tag{22}$$

is the modified Reynolds number

$$\begin{aligned}
&\rho^{\circledast} = 1 - \lambda^{\circledast}\left(T^{\circledast} - 1.0\right), \mu^{\circledast} = \exp\left[-\beta^{\circledast}\left(T^{\circledast} - 1.0\right)\right],\\
&\rho_{\text{av}}^{\circledast} = 1 - \lambda^{\circledast}\left(T_{\text{av}}^{\circledast} - 1.0\right), \rho_{\text{av}}^{\circledast} = 1 - \lambda^{\circledast}\left(T_{\text{av}}^{\circledast} - 1.0\right),\\
&\mu_{\text{av}}^{\circledast} = \exp\left[-\beta^{\circledast}\left(T_{\text{av}}^{\circledast} - 1.0\right)\right], h^{\circledast} = 1 - x^{\circledast}(1 - w), w = \frac{h_0}{h_i} \le 1.
\end{aligned} \tag{23}$$

Boundary conditions are as follows: $\bar{p}^{\circledast} = 0$ at $x^{\circledast} = 0$ and $\bar{p}^{\circledast} = 0$ at $x^{\circledast} = 1$, $u^{\circledast} = 1$, and $v^{\circledast} = 0$, on the moveable slider, and $u^{\circledast} = v^{\circledast} = 0$ on the stationary pad of the bearing.

The following boundary conditions for the temperature of unsteady fluid flow are used for the energy equation: $T^{\circledast} = T^s$ on the moveable slider, $T^{\circledast} = T^p$ on the stationary pad, and $T^{\circledast} = T^i$ at the inlet of slider $(x^{\circledast} = 0)$, where

$$\begin{aligned}
&T^p = T^i = T^s,\\
&T^i < T^s < T^p,\\
&T^i < T^p < T^s.
\end{aligned} \tag{24}$$

For computation purposes, the irregular domain of the slider bearing for unsteady fluid flow lubricant is transformed into a regular geometric domain, according to Sinha and Adamu [18]. Assuming the roughness on the pad and runner to be identical random distributions $(\delta_1 = \delta_2)$, the following linear transformation was chosen:

$$\begin{aligned}
&y^{\circledast} = y^{\dagger}h^{\circledast}\left(x^{\dagger}\right) + \delta_1^{\circledast},\\
&0 \le y^{\dagger} \le 1.
\end{aligned} \tag{25}$$

The decoupled main governing equations of unsteady lubricant of (17), (18), (19), (20), and (21) become

$$\begin{aligned}
&\rho_{\text{av}}^{\circledast}\left(D_1\frac{d^2p^{\circledast}}{dx^{\dagger 2}}\right) + \left[-\lambda^{\circledast}\frac{\partial T_{\text{av}}^{\circledast}}{\partial x^{\dagger}}D_1 + \rho_{\text{av}}^{\circledast}\left(\beta^{\circledast}\frac{\partial T_{\text{av}}^{\circledast}}{\partial x^{\dagger}}D_1 + D_2\frac{dh^{\circledast}}{dx^{\dagger}}\right)\right]\frac{dp^{\circledast}}{dx^{\dagger}}\\
&= 6\mu_{\text{av}}^{\circledast}\left(\rho_{\text{av}}^{\circledast}\frac{dh^{\circledast}}{dx^{\circledast}} - \lambda^{\circledast}h^{\circledast}\frac{\partial T_{\text{av}}^{\circledast}}{\partial x^{\dagger}}\right) + BD_3\,\text{Re}^{\circledast}\rho_{\text{av}}^{\circledast},
\end{aligned} \tag{26}$$

$$\begin{aligned}
&-\lambda^{\circledast}\frac{\partial T_{\text{av}}^{\circledast}}{\partial x^{\dagger}}D_4\frac{dp^{\circledast}}{dx^{\dagger}} + \rho_{\text{av}}^{\circledast}\frac{dp^{\circledast}}{dx^{\dagger}}\left(\beta^{\circledast}\frac{\partial T_{\text{av}}^{\circledast}}{\partial x^{\dagger}}D_4 + D_5\frac{dh^{\circledast}}{dx^{\dagger}}\right)\\
&\quad + D_4\rho_{\text{av}}^{\circledast}\frac{d^2p^{\circledast}}{dx^{\dagger 2}} = 6\mu_{\text{av}}^{\circledast}\left(\rho_{\text{av}}^{\circledast}D_6\frac{dh^{\circledast}}{dx^{\dagger}} - \lambda^{\circledast}D_7\frac{\partial T_{\text{av}}}{\partial x^{\dagger}}\right)\\
&\quad + BD_3\text{Re}^{\circledast}\rho_{\text{av}}^{\circledast},
\end{aligned} \tag{27}$$

$$\frac{1}{h^{\circledast 2}}\mu^{\circledast}\left(-\beta^{\circledast}\frac{\partial T^{\circledast}}{\partial y^{\dagger}}\frac{\partial u\circledast}{\partial y^{\dagger}}+\frac{\partial^2 u^{\circledast}}{\partial y^{\dagger 2}}\right)=\frac{dp^{\circledast}}{dx^{\dagger}}+\mathrm{Re}^{\circledast}$$
$$\cdot\left[-\lambda u^{\circledast}\frac{\partial T^{\circledast}}{\partial t^{\dagger}}+\rho^{\circledast}\frac{\partial u^{\circledast}}{\partial t^{\dagger}}-\lambda^{\circledast}u^{\circledast 2}\frac{\partial T^{\circledast}}{\partial x^{\dagger}}+\rho^{\circledast}u^{\circledast}\frac{\partial u^{\circledast}}{\partial x^{\dagger}}\right.$$
$$+\frac{\lambda^{\circledast}u^{\circledast 2}}{h^{\circledast}}y^{\dagger}\frac{dh^{\circledast}}{dx^{\dagger}}\frac{\partial T^{\circledast}}{\partial y^{\dagger}}-\frac{\rho^{\circledast}u^{\circledast}}{h^{\circledast}}y^{\dagger}\frac{dh^{*}}{dx^{\dagger}}\frac{\partial u^{\circledast}}{\partial y^{\dagger}}$$
$$\left.-\frac{\lambda^{\circledast}v^{\circledast}u^{\circledast}}{h^{\circledast}}\frac{\partial T^{\circledast}}{\partial y^{\dagger}}+\frac{\rho^{\circledast}v^{\circledast}}{h^{\circledast}}\frac{\partial u^{\circledast}}{\partial y^{\dagger}}\right]. \tag{28}$$

$$-\lambda^{\circledast}u^{\circledast}\frac{\partial T^{\circledast}}{\partial x^{\dagger}}+\rho^{\circledast}\frac{\partial u^{\circledast}}{\partial x^{\dagger}}+\frac{\lambda^{\circledast}}{h^{\circledast}}y^{\dagger}\frac{dh^{\circledast}}{dx^{\dagger}}u^{\circledast}\frac{\partial T^{\circledast}}{\partial y^{\dagger}}-\frac{\rho^{\circledast}}{h^{\circledast}}y^{\dagger}\frac{dh^{*}}{dx^{\dagger}}\frac{\partial u^{\circledast}}{\partial y^{\dagger}}$$
$$-\frac{\lambda^{\circledast}}{h^{\circledast}}v^{\circledast}\frac{\partial T^{\circledast}}{\partial y^{\dagger}}+\frac{\rho^{\circledast}}{h^{\circledast}}\frac{\partial v^{\circledast}}{\partial y^{\dagger}}=0, \tag{29}$$

$$\rho^{\circledast}\left[u^{\circledast}\left(\frac{\partial T^{\circledast}}{\partial x^{\dagger}}-\frac{1}{h^{\circledast}}y^{\dagger}\frac{dh^{\circledast}}{dx^{\dagger}}\frac{\partial T^{\circledast}}{\partial y^{\dagger}}\right)+\frac{1}{h^{\circledast}}v^{\circledast}\frac{\partial T^{\circledast}}{\partial y^{\dagger}}\right]$$
$$=\frac{1}{p_e h^{\circledast 2}}\frac{\partial^2 T^{\circledast}}{\partial y^{\dagger 2}}+\frac{p_r E_c\mu^{\circledast}}{p_e h^{\circledast 2}}\left(\frac{\partial u^{\circledast}}{\partial y^{\dagger}}\right)^2+\frac{p_r E_c u^{\circledast}}{p_e}\frac{dp^{\circledast}}{dx^{\dagger}}. \tag{30}$$

where

$D_1=h^{\circledast 3}+3h^{\circledast}\sigma^{\circledast 2}, D_2=3h^{\circledast 2}+3\sigma^{\circledast 2}, D_3=h^{\circledast 2}+\sigma^{\circledast 2}$, $D_4=h^{\circledast 3}-6h^{\circledast}\sigma^{\circledast 2}, D_5=3h^{\circledast 2}-6\sigma^{\circledast 2}, D_6=1+3(\sigma^{\circledast 2}/h^{\circledast 2})$, $D_7=h^{\circledast}-3(\sigma^{\circledast 2}/h^{\circledast})$,

$$B=-\lambda^{\circledast}\frac{\partial h^{\circledast}}{\partial x^{\dagger}}\frac{\partial T^{\circledast}_{av}}{\partial t^{\dagger}}-\lambda^{\circledast}h^{\circledast}\frac{\partial^2 T^{\circledast}_{av}}{\partial x^{\dagger}\partial t^{\dagger}}-2\lambda^{\circledast}U^{\circledast}_m\frac{\partial h^{\circledast}}{\partial x^{\dagger}}\frac{\partial T^{\circledast}_{av}}{\partial x^{\dagger}}$$
$$-\lambda^{\circledast}h^{\circledast}U^{\circledast}_m\frac{\partial^2 T^{\circledast}_{av}}{\partial x^{\dagger 2}}-\lambda^{\circledast}h^{\circledast}\frac{\partial U^{\circledast}_m}{\partial x^{\dagger}}\frac{\partial T^{\circledast}_{av}}{\partial x^{\dagger}}+\lambda^{\circledast}U^{\circledast}_m\frac{\partial h^{\circledast}}{\partial x^{\dagger}}\frac{\partial T^{\circledast}_{av}}{\partial t^{\dagger}}$$
$$+\lambda^{\circledast}h^{\circledast}\frac{\partial U^{\circledast}_m}{\partial x^{\dagger}}\frac{\partial T^{\circledast}_{av}}{\partial t^{\dagger}}+\lambda^{\circledast}h^{\circledast}U^{\circledast}_m\frac{\partial^2 T^{\circledast}_{av}}{\partial x^{\dagger}\partial t^{\dagger}}+\lambda^{\circledast}h^{\circledast}\frac{\partial T^{\circledast}_{av}}{\partial x^{\dagger}}\frac{\partial U^{\circledast}_m}{\partial t^{\dagger}}$$
$$+4\lambda^{\circledast}h^{\circledast}\frac{\partial U^{\circledast}_m}{\partial x^{\dagger}}\frac{\partial T^{\circledast}_{av}}{\partial x^{\dagger}}-2\lambda^{\circledast}U^{\circledast 2}_m\frac{\partial h^{\circledast}}{\partial x^{\dagger}}\frac{\partial T^{\circledast}_{av}}{\partial x^{\dagger}}+\rho^{\circledast}_{av}\frac{\partial h^{\circledast}}{\partial x^{\dagger}}\frac{\partial U^{\circledast}_m}{\partial x^{\dagger}}$$
$$+h^{\circledast}\rho^{\circledast}_{av}\frac{\partial^2 U^{\circledast}_m}{\partial x^{\dagger 2}}-\rho^{\circledast}_{av}\frac{\partial h^{\circledast}}{\partial x^{\dagger}}\frac{\partial U^{\circledast}_m}{\partial t^{\dagger}}-\rho^{\circledast}_{av}h^{\circledast}\frac{\partial^2 U^{\circledast}_m}{\partial x^{\dagger}\partial t^{\dagger}}$$
$$-4\rho^{\circledast}_{av}\frac{\partial h^{\circledast}}{\partial x^{\dagger}}\frac{\partial U^{\circledast}_m}{\partial x^{\dagger}}-2h^{\circledast}\rho^{\circledast}_{av}\frac{\partial^2 U^{\circledast}_m}{\partial x^{\dagger 2}}-h^{\circledast}U^{\circledast 2}_m\frac{\partial^2 T^{\circledast}_{av}}{\partial x^{\dagger 2}}.$$

The transformed dimensionless temperature-dependent viscosity and density equations are as follows:

$$\rho^{\circledast}=1.0-\lambda^{\circledast}\left(T^{\circledast}-1.0\right).\mu^{\circledast}=\exp\left(-\beta^{\circledast}\left(T^{\circledast}-1.0\right)\right),$$
$$\rho^{\circledast}_{\mathrm{av}}=1.0-\lambda^{\circledast}\left(T^{\circledast}_{\mathrm{av}}-1.0\right).\mu^{\circledast}_{\mathrm{av}}=\exp\left(-\beta^{\circledast}\left(T^{\circledast}_{\mathrm{av}}-1.0\right)\right), \tag{31}$$

where $T^{\circledast}_{\mathrm{av}}=\int_0^1 T^{\circledast}dy^{\dagger}$.

The following initial essential boundary conditions are tokens for this article:

$$u^{\circledast}=1-y^{\dagger}, v^{\circledast}=0 \text{ at } x^{\dagger}=0, U^{\circledast}(x,y,0)$$
$$=U^{\circledast}(x,y), T^{\circledast}(x,y,0)=T^{\circledast}(x,y). \tag{32}$$

The dimensionless load-carrying capacity performance $W^{\circledast}$ and the drag force $F^{\circledast}$ are obtained from the following equations, respectively:

$$W^{\circledast}=\frac{Wh_i^2}{\mu_a UB^2}=\int_0^1 p^{\circledast}\,dx^{\dagger},$$
$$F^{\circledast}=\frac{Fh_i}{\mu_a UB}=\int_0^1\left(\mu^{\circledast}\frac{\partial u^{\circledast}}{h^{\circledast}\partial y^{\dagger}}\right)_{y^{\dagger}=0}dx^{\dagger}. \tag{33}$$

3. Finite Element Formulation

In order to obtain the weak form of the aforementioned equations for finite element formulation, we first form the weighted integral equations for (26), (27), (29), and (30) and apply integration by parts to the terms with second derivatives. Bilinear rectangular elements are used for governing.

Let the geometry of the domain Ω be divided into N_e bilinear rectangular elements, and $\bar{\Omega}=\Omega\cup\Gamma$.

$$\cup_{e=1}^{N_e}\bar{\Omega}_e=\bar{\Omega},$$
$$\cap_{e=1}^{N_e}\bar{\Omega}_e=\varnothing, \tag{34}$$

where N_e discretized number of rectangular elements, Ω_e denotes the interior domain of an element, and Γ_e is the boundary of rectangular element Ω_e.

The elemental weak form of the governing Eqs. (26), (27), (29), (30), and (31) is as follows:

$$\int_{\Omega^e}\left[-\rho^{\circledast}_{\mathrm{av}}\left(D_1\frac{dN_i}{dx^{\dagger}}\frac{dp^{\circledast}}{dx^{\dagger}}\right)+N_i\left[-\lambda^{\circledast}\frac{\partial T^{\circledast}_{\mathrm{av}}}{\partial x}D_1\right.\right.$$
$$\left.\left.+\rho^{\circledast}_{\mathrm{av}}\left(\beta^{\circledast}\frac{\partial T^{\circledast}_{\mathrm{av}}}{\partial x^{\dagger}}D_1+D_2\frac{dh^{\circledast}}{dx^{\dagger}}\right)\right]\frac{dp^{\circledast}}{dx^{\dagger}}\right]d\Omega$$
$$=\int_{\Omega^e}\left[6N_i\mu^{\circledast}_{\mathrm{av}}\left(\rho^{\circledast}_{\mathrm{av}}\frac{dh^{\circledast}}{dx^{\dagger}}-\lambda^{\circledast}h^{\circledast}\frac{\partial T^{\circledast}_{\mathrm{av}}}{\partial x^{\dagger}}\right)+BD_3N_i\,\mathrm{Re}^{\circledast}\rho^{\circledast}_{\mathrm{av}}\right]d\Omega, \tag{35}$$

$$\int_{\Omega^e}\left[-\rho^{\circledast}_{\mathrm{av}}\left(D_4\frac{dN_i}{dx^{\dagger}}\frac{dp^{\circledast}}{dx^{\dagger}}\right)+N_i\left[-\lambda^{*}\frac{\partial T^{\circledast}_{\mathrm{av}}}{\partial x^{\dagger}}D_4\right.\right.$$
$$\left.\left.+\rho^{\circledast}_{\mathrm{av}}\left(\beta^{\circledast}\frac{\partial T^{\circledast}_{\mathrm{av}}}{\partial x^{\dagger}}D_4\right)+D_5\frac{dh^{\circledast}}{dx^{\dagger}}\right]\frac{dp^{\circledast}}{dx^{\dagger}}-BD_3\,\mathrm{Re}^{\circledast}N_i\rho^{\circledast}_{\mathrm{av}}\right]d\Omega$$
$$=\int_{\Omega^e}\left[6N_i\mu^{\circledast}_{\mathrm{av}}\left(\rho^{\circledast}_{\mathrm{av}}D_6\frac{dh^{\circledast}}{dx^{\dagger}}-\lambda^{\circledast}D_7\frac{\partial T^{\circledast}_{\mathrm{av}}}{\partial x^{\dagger}}\right)\right]d\Omega, \tag{36}$$

$$\int_{\Omega^e}\left[-\frac{\mu^{\circledast}}{h^{\circledast 2}}\left(\frac{\partial N_i}{\partial y^{\dagger}}\frac{\partial u^{\circledast}}{\partial y^{\dagger}}+\beta N_i\frac{\partial T^{\circledast}}{\partial y^{\dagger}}\frac{\partial u^{\circledast}}{\partial y^{\dagger}}\right)\right.$$
$$-N_i\frac{dp^{\circledast}}{dx^{\dagger}}+N_i\,\mathrm{Re}^{\circledast}\left(\lambda u^{\circledast}\frac{\partial T^{\circledast}}{\partial t^{\dagger}}-\rho^{\circledast}\frac{\partial u^{\circledast}}{\partial t^{\dagger}}+\lambda^{\circledast}u^{\circledast 2}\frac{\partial T^{\circledast}}{\partial x^{\dagger}}\right.$$
$$-\rho^{\circledast}u^{\circledast}\frac{\partial u^{\circledast}}{\partial x^{\dagger}}-\frac{\lambda^{\circledast}u^{\circledast 2}}{h^{\circledast}}y^{\dagger}\frac{dh^{\circledast}}{dx^{\dagger}}\frac{\partial T^{\circledast}}{\partial y^{\dagger}}+\frac{\rho^{\circledast}u^{\circledast}}{h^{\circledast}}y^{\dagger}\frac{dh^{*}}{dx^{\dagger}}\frac{\partial u^{\circledast}}{\partial y^{\dagger}}$$
$$\left.\left.+\frac{\lambda^{\circledast}v^{\circledast}u^{\circledast}}{h^{\circledast}}\frac{\partial T^{\circledast}}{\partial y^{\dagger}}-\frac{\rho^{\circledast}v^{\circledast}}{h^{\circledast}}\frac{\partial u^{\circledast}}{\partial y^{\dagger}}\right)\right]d\Omega=0, \tag{37}$$

$$\int_{\Omega^e} N_i \left[-\lambda^{\circledast} u^{\circledast} \frac{\partial T^{\circledast}}{\partial x^{\dagger}} + \rho^{\circledast} \frac{\partial u^{\circledast}}{\partial x^{\dagger}} + \frac{\lambda^{\circledast}}{h^{\circledast}} y^{\dagger} \frac{dh^{\circledast}}{dx^{\dagger}} u^{\circledast} \frac{\partial T^{\circledast}}{\partial y^{\dagger}} - \frac{\rho^{\circledast}}{h^{\circledast}} y^{\dagger} \frac{dh^{*}}{dx^{\dagger}} \frac{\partial u^{\circledast}}{\partial y^{\dagger}} - \lambda^{\circledast} v^{\circledast} \frac{\partial T^{\circledast}}{\partial y^{\dagger}} + \rho^{\circledast} \frac{\partial v^{\circledast}}{\partial y^{\dagger}} \right] d\Omega = 0, \tag{38}$$

$$\begin{aligned} &\int_{\Omega^e} \left[\rho^{\circledast} N_i \left[u^{\circledast} \left(\frac{\partial T^{\circledast}}{\partial x^{\dagger}} - \frac{y^{\dagger}}{h^{\circledast}} \frac{dh^{\circledast}}{dx^{\dagger}} \frac{\partial T^{\circledast}}{\partial y^{\dagger}} \right) + \frac{v^{\circledast}}{h^{\circledast}} \frac{\partial T^{\circledast}}{\partial y^{\dagger}} \right] \right. \\ &\quad \left. - \frac{1}{p_e h^{\circledast 2}} \frac{\partial N_i}{\partial y^{\dagger}} \frac{\partial T^{\circledast}}{\partial y^{\dagger}} - \frac{P_r E_c \mu^{\circledast}}{P_e h^{\circledast 2}} N_i \left(\frac{\partial u^{\circledast}}{\partial y^{\dagger}} \right)^2 \right] d\Omega \\ &\quad - \int_{\Omega^e} \frac{P_r E_c u^{\circledast}}{P_e} N_i \frac{dp^{\circledast}}{dx^{\dagger}} d\Omega = 0, \end{aligned} \tag{39}$$

where N_i is the weight (or test) for one- and two-dimensional functions. To generalize the finite element formulation, it is assumed that the same order of polynomials is used to approximate velocity, temperature, average temperature, and $U_m^{\circledast}$ unknowns and different for pressure unknown weight function, i.e.,

$$\begin{aligned} u^{\circledast}(x^{\dagger}, y^{\dagger}, t^{\dagger}) &\approx \sum_{j=1}^{\text{nel}} u_j(t^{\dagger}) \Phi_j(x^{\dagger}, y^{\dagger}), & v^{\circledast}(x^{\dagger}, y^{\dagger}) &\approx \sum_{j=1}^{\text{nel}} v_j \Phi_j(x^{\dagger}, y^{\dagger}), \\ P^{\circledast}(x^{\dagger}) &\approx \sum_{j=1}^{\text{nel}} P_j \Phi_j(x^{\dagger}), & T^{\circledast}(x^{\dagger}, y^{\dagger}) &\approx \sum_{j=1}^{\text{nel}} T_j \Phi_j(x^{\dagger}, y^{\dagger}), \\ T_{\text{av}}^{\circledast}(y^{\dagger}, t^{\dagger}) &\approx \sum_{j=1}^{\text{nel}} T_{\text{av}j} \Phi_j(y^{\dagger}), & U_m^{\circledast}(y^{\dagger}, t^{\dagger}) &\approx \sum_{j=1}^{\text{nel}} U_{mj} \Phi_j(y^{\dagger}), \end{aligned} \tag{40}$$

where U_j, V_j, P_j, T_j, T_{av}, and U_m are nodal unknown values and Φ_j are shape (basis) functions of space variables only that are used to construct the approximate solutions. nel is the pressure, velocity, and temperature number of nodes over an element, i.e., nel = 2 for P, T_{av}, and U_m and nel = 4 for U, V, and T. In consideration of GFEM, the selection of weight functions is the same as the shape functions $(N_i = \Phi_j)$.

Due to the node-to-node oscillatory solutions of the Galerkin finite element method (GFEM), instead, streamline upwind Petrov-Galerkin (SUPG) was used for U, V, and T. The weighted residual formulation of the above equation is obtained by substituting the approximation equation (40) into (35), (36), (37), (38), and (39). Thus, the weak integral form of P and the SUPG decoupled governing equations for U, V, and T are as follows:

$$\begin{aligned} &\sum_{j=1}^{\text{nel}} \left[\int_{\Omega^e} \left(-\rho_{\text{av}}^{\circledast} D_1 \frac{dN_i}{dx^{\dagger}} \frac{d\Phi_j}{dx^{\dagger}} + \tilde{N}_i \left(-\lambda^{\circledast} \frac{dT_{\text{av}}^{\circledast}}{dx^{\dagger}} D_1 \right. \right. \right. \\ &\quad \left. \left. \left. + \rho_{\text{av}}^{\circledast} \left[\beta^{*} \frac{dT_{\text{av}}^{\circledast}}{dx^{\dagger}} D_1 + D_2 \frac{dh^{\circledast}}{dx^{\dagger}} \right] \right) \frac{d\Phi_j}{dx^{\dagger}} \right) d\Omega \right] P_j \\ &= \int_{\Omega^e} \left[6\tilde{N}_i \mu_{\text{av}}^{\circledast} \left(\rho_{\text{av}}^{\circledast} \frac{dh^{\circledast}}{dx^{\dagger}} - \lambda^{\circledast} h^{\circledast} \frac{dT_{\text{av}}^{\circledast}}{dx^{\dagger}} \right) + BD_3 \operatorname{Re}^{\circledast} \tilde{N}_i \rho_{\text{av}}^{\circledast} \right] d\Omega, \end{aligned} \tag{41}$$

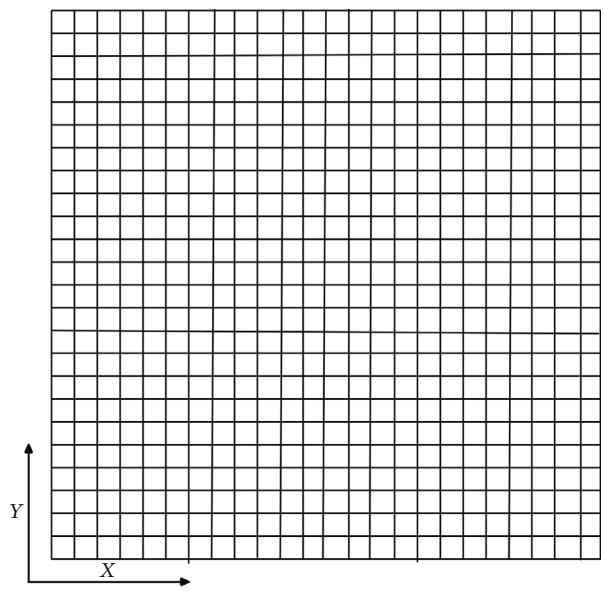

Figure 2: Regular domain discretization system of grid.

$$\begin{aligned} &\sum_{j=1}^{\text{nel}} \left[\int_{\Omega^e} \left(-\rho_{\text{av}g}^{\circledast} D_4 \frac{dN_i}{dx^{\dagger}} \frac{d\Phi_j}{dx^{\dagger}} + \tilde{N}_i \left(-\lambda^{\circledast} \frac{dT_{\text{av}}^{\circledast}}{dx^{\dagger}} D_4 \right. \right. \right. \\ &\quad \left. \left. \left. + \rho_{\text{av}}^{\circledast} \left[\beta^{\circledast} \frac{dT_{\text{av}}^{\circledast}}{dx^{\dagger}} D_4 + D_5 \frac{dh^{\circledast}}{dx^{\dagger}} \right] \frac{d\Phi_j}{dx^{\dagger}} \right) \right) d\Omega \right] P_j \\ &= \int_{\Omega^e} \left[6\tilde{N}_i \mu_{\text{av}}^{\circledast} \left(\rho_{\text{av}}^{\circledast} D_6 \frac{dh^{\circledast}}{dx^{\dagger}} - \lambda^{\circledast} D_7 \frac{\partial T_{\text{av}}^{\circledast}}{\partial x^{\dagger}} \right) + \operatorname{Re}^{\circledast} \tilde{N}_i B \left[\rho_{\text{av}}^{\circledast} \left(h^{\circledast 2} + \sigma^{\circledast 2} \right) \right] \right] d\Omega, \end{aligned} \tag{42}$$

$$\begin{aligned} &\sum_{j=1}^{\text{nel}} \left[\int_{\Omega^e} - \tilde{N}_i \rho^{\circledast} \operatorname{Re}^{\circledast} \Phi_j d\Omega \right] \frac{\partial U_j^{\circledast}}{\partial t^{\dagger}} \\ &\quad + \sum_{j=1}^{\text{nel}} \left[\int_{\Omega^e} \left(-\frac{\mu^{\circledast}}{h^{\circledast 2}} \left[\tilde{N}_i \beta \frac{\partial \Phi_j}{\partial y^{\dagger}} \frac{\partial \Phi_j}{\partial y^{\dagger}} \sum_{k=1}^{\text{nel}} T_k + \frac{\partial N_i}{\partial y^{\dagger}} \frac{\partial \Phi_k}{\partial y^{\dagger}} \right] \right. \right. \\ &\quad \left. \left. + \tilde{N}_i \operatorname{Re}^{\circledast} \left(-\rho^{\circledast} u_o^{\circledast} \frac{\partial \Phi_j}{\partial x^{\dagger}} + \frac{\rho^{\circledast} u_o^{\circledast}}{h^{\circledast}} y^{\dagger} \frac{dh^{*}}{dx^{\dagger}} \frac{\partial \Phi_j}{\partial y^{\dagger}} - \frac{\rho^{\circledast} v_o^{\circledast}}{h^{\circledast}} \frac{\partial \Phi_j}{\partial y^{\dagger}} \right) \right) d\Omega \right] U_j \\ &= \int_{\Omega^e} \left[\frac{d\Phi_j}{dx^{\dagger}} \sum_{k=1}^{\text{nel}} P_k + \operatorname{Re}^{\circledast} \left(-\lambda^{\circledast} u_o^{\circledast} \frac{\partial \Phi_j}{\partial t^{\dagger}} \sum_{k=1}^{\text{nel}} T_k - \lambda^{\circledast} u_o^{\circledast 2} \frac{\partial \Phi_j}{\partial x^{\dagger}} \sum_{k=1}^{\text{nel}} T_k \right. \right. \\ &\quad \left. \left. + \frac{\lambda^{\circledast} u_o^{\circledast 2}}{h^{\circledast}} y^{\dagger} \frac{dh^{\circledast}}{dx^{\dagger}} \frac{\partial \Phi_j}{\partial y^{\dagger}} \sum_{k=1}^{\text{nel}} T_k - \frac{\lambda^{\circledast} v_o^{\circledast} u_o^{\circledast}}{h^{\circledast}} \frac{\partial \Phi_j}{\partial y^{\dagger}} \sum_{k=1}^{\text{nel}} T_k \right) \right] \tilde{N}_i d\Omega, \end{aligned} \tag{43}$$

$$\begin{aligned} &\sum_{j=1}^{\text{nel}} \left[\int_{\Omega^e} \left(-\frac{\Phi_z}{h^{\circledast}} \lambda^{\circledast} \frac{\partial \Phi_j}{\partial y^{\dagger}} + \frac{\rho^{\circledast}}{h^{\circledast}} \frac{\partial \Phi_j}{\partial y^{\dagger}} \right) \tilde{N}_i d\Omega \right] V_j \\ &= \int_{\Omega^e} \left[\lambda^{\circledast} u_0^{\circledast} \frac{\partial \Phi_j}{\partial x^{\dagger}} \sum_{k=1}^{\text{nel}} T_k - \rho^{\circledast} \frac{\partial \Phi_z}{\partial x^{\dagger}} \sum_{k=1}^{\text{nel}} U_k + \frac{\lambda^{\circledast}}{h^{\circledast}} y^{\dagger} \frac{dh^{\circledast}}{dx^{\dagger}} u_0^{\circledast} \frac{\partial \Phi_z^{\circledast}}{\partial y^{\dagger}} \sum_{k=1}^{\text{nel}} T_k \right. \\ &\quad \left. - \frac{\rho^{\circledast}}{h^{\circledast}} y^{\dagger} \frac{dh^{*}}{dx^{\dagger}} \frac{\partial \Phi_z^{\circledast}}{\partial y^{\dagger}} \sum_{k=1}^{\text{nel}} U_k \right] \tilde{N}_i d\Omega, \end{aligned} \tag{44}$$

Step 1. Initialization.
i. Input the constant data value: $\lambda^{\circledast}, \beta^{\circledast}, \sigma^{\circledast}, P_r, E_c, P_e, Re^{\circledast}$
ii. Fix all boundary conditions for $u^{\circledast}, v^{\circledast}, T^{\circledast}, P^{\circledast}$,
iii. Fix fictitious values for $u^{\circledast}, v^{\circledast}, T^{\circledast}, P^{\circledast}$ over the entire grid points
Step 2. Calculate $p^{\circledast\text{new}}$ using Eq. (41) or (42).
Step 3. Calculate $u^{\circledast\text{new}}$ using $p^{\circledast\text{new}}$, $u^{\circledast\text{old}}$, $v^{\circledast\text{old}}$ and $T^{\circledast\text{old}}$ and Eq. (43).
Step 4. Calculate $v^{\circledast\text{new}}$ using $u^{\circledast\text{new}}$, $v^{\circledast\text{old}}$ and $T^{\circledast\text{old}}$ and Eq. (44).
Step 5. Calculate $T^{\circledast\text{new}}$ using $p^{\circledast\text{new}}$, $u^{\circledast\text{new}}$, $v^{\circledast\text{new}}$ and $T^{\circledast\text{old}}$ and Eq. (45).
Step 6. Test the convergence rate.
Step 7. Repeat steps 2-6 till convergence is obtained for all spatial variables.
Step 8. Calculate load carrying capacity performance $W^{\circledast}$ and friction force $F^{\circledast}$ using Eq. (33).

Algorithm 1: General steps to solve the governing equation.

$$\sum_{j=1}^{\text{nel}}\left[\int_{\Omega^e}\left(\tilde{N}_i\rho^{\circledast}\left(u_0^{\circledast}\frac{\partial \text{m}_j}{\partial x^{\dagger}}-\frac{y^{\dagger}}{h^{\circledast}}\frac{dh^{\circledast}}{dx^{\dagger}}\frac{\partial \text{m}_j}{\partial y^{\dagger}}+\frac{v_0^{\circledast}}{h^{\circledast}}\frac{\partial \text{m}_j}{\partial y^{\dagger}}\right)+\frac{1}{P_e h^{\circledast 2}}\frac{\partial N_i}{\partial y^{\dagger}}\frac{\partial \text{m}_j}{\partial y^{\dagger}}\right)d\Omega\right]T_j=\int_{\Omega^e}\tilde{N}_i\left[\frac{P_rE_c\mu^{\circledast}}{P_e h^{\circledast 2}}\left(\frac{\partial \text{m}_z}{\partial y^{\dagger}}\sum_{k=1}^{\text{nel}}U_k\right)^2+\frac{P_rE_c}{P_e}u_0\frac{\partial \text{m}_z}{\partial x^{\dagger}}\sum_{k=1}^{\text{nel}}P_k\right]d\Omega, \tag{45}$$

where $\tilde{N}_i$ is the SUPG weight (or test) function expressed as

$$\tilde{N}_i=\text{m}_i+S_i,\ S_i=\frac{\bar{k}\tilde{u}_j\text{m}_{i,j}}{\|u\|}. \tag{46}$$

$\tilde{k}$ is the SUPG upwind parameter calculated using elemental dimensions and elemental unknown to the center of quadrilateral elements. The most detailed explanation is given by Brooks and Hughes [33]. Since we are using a linear shape and weight function, terms of $T_{\text{av}}^{\circledast}$ and $U_m^{\circledast}$ in (41) and (42) that have a second-order derivative go to zero.

3.1. Treatment of the Solution. Figure 2 shows a 25×25 grid discretization mesh for finite element for numerical computation for temperature and velocity, whereas for pressure, average temperature, and U_m, only the bottom one-dimensional line of the x-axis is used in this article.

Equation (43) includes nodal unknowns and time derivatives. Therefore, it is not a set of algebraic equations but instead a set of ODEs. First, SUPG-FEM was developed using a semidiscrete formulation, and the Crank-Nicolson schemes were applied to solve the system of equations for time-dependent equation. Because the remaining equations (41), (42), (44), and (45) contain nonlinear terms, the formulated system of algebraic equations is solved iteratively.

The approximated SUPG-FEM solution obtained for the above equation is to an accuracy of tolerance (Tol), where the error is calculated as

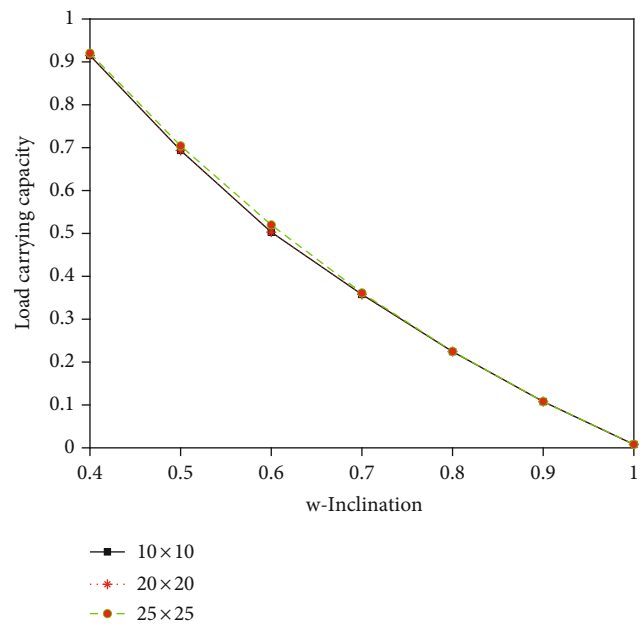

Figure 3: LCCP vs. inclination on different grid system.

$$\max\left[\frac{\left|\psi_j^{\text{new}}-\psi_j^{\text{prev}}\right|}{\left|\psi_j^{\text{new}}\right|}\right]<\text{Tol}, \tag{47}$$

and ψ_j are values of the unknown nodal variables at coordinate points.

(Tol) = 10^{-3}, 10^{-4}, and 10^{-5} tolerance were used for iterations performed. However, on approximate solution, there is no significant difference for all different values of tolerance. MATLAB software version 2021 is used to obtain the result by developing MATLAB code. Algorithm 1 shows the general steps to solve the governing equation to obtain the result.

4. Results and Discussion

The tilted slider plane bearing parameters for time-dependent fluid flow lubricant in this article appear to be functions of the dimensionless parameters P_e, P_r, and E_c as well as $\gamma^{\circledast}$, $\eta^{\circledast}$, w, $\text{Re}^{\circledast}$, and $\sigma^{\circledast}$. The following parameter

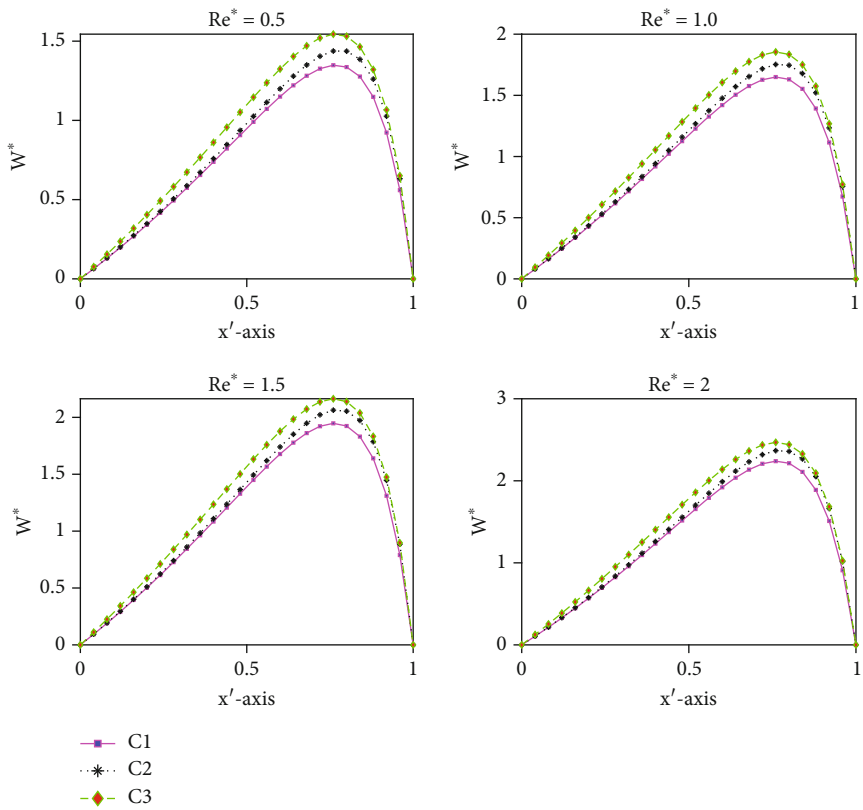

Figure 4: Pressure distributions at $T^i = T^p = T^s = 1.0$, $w = 0.4$ and for different value of $\mathrm{Re}^{\circledast}$ (longitudinal roughness).

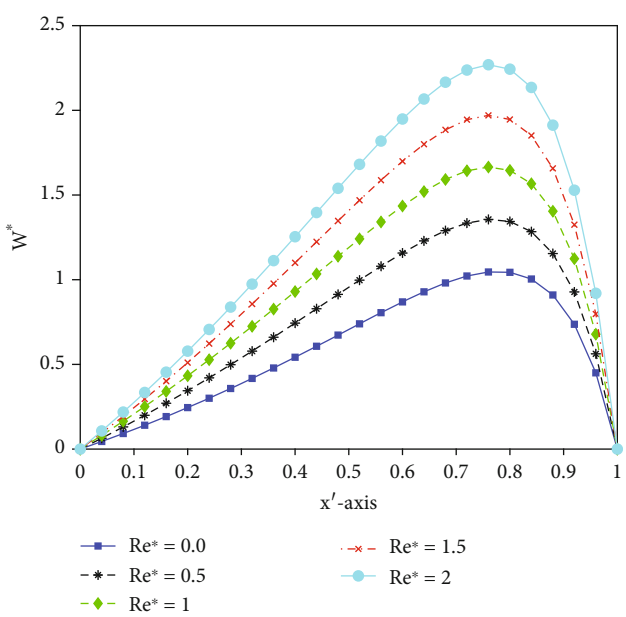

Figure 5: Pressure distributions at $w = 0.4$ and for different values of $\mathrm{Re}^{\circledast}$.

values were selected in accordance with the Lebeck consideration stated in [34].

Some other constants are given in detail in Sinha and Adamu [18]. The findings on pressure distribution, load-bearing capacity performance, drag friction force, velocity, and temperature performance have been investigated.

Table 1: Longitudinal roughness $W^{\circledast}$ and $F^{\circledast}$ for condition(C_1) at different values of $\mathrm{Re}^{\circledast}$ and w.

	w	0.4	0.6	0.8	1
$\mathrm{Re}^{\circledast} = 0.5$	$W^{\circledast}$	0.7697	0.4114	0.1659	0.0025
	$F^{\circledast}$	1.6959	1.3197	1.1151	1.0000
$\mathrm{Re}^{\circledast} = 1$	$W^{\circledast}$	0.9475	0.5297	0.2221	0.0037
	$F^{\circledast}$	1.7422	1.3320	1.1147	0.9998
$\mathrm{Re}^{\circledast} = 1.5$	$W^{\circledast}$	1.0745	0.6421	0.2751	0.0048
	$F^{\circledast}$	1.7868	1.3433	1.1139	0.9994
$\mathrm{Re}^{\circledast} = 2$	$W^{\circledast}$	1.2792	0.7479	0.3243	0.0057
	$F^{\circledast}$	1.8293	1.3534	1.1128	0.9988

The results obtained are illustrated using tables and graphs. To ensure domain discretization grid independence, the numerical simulations were run on various grid systems with 10 by 10, 20 by 20, and 25 by 25 grid points. The load-carrying capacity performance of various grids is compared and displayed in Figure 3. This leads to the conclusion that the grid scheme of 25 by 25 produces a grid-independent solution. Finally, the bearing performance is calculated from equation (33) using the trapezoidal method.

Table 2: Longitudinal roughness $W^{\circledast}$ and $F^{\circledast}$ for condition(C_2) at different values of $Re^{\circledast}$ and w.

	w	0.4	0.6	0.8	1
$Re^{\circledast} = 0.5$	$W^{\circledast}$	0.8122	0.4282	0.1712	0.0025
	$F^{\circledast}$	1.7070	1.3209	1.1150	1.0000
$Re^{\circledast} = 1$	$W^{\circledast}$	0.9960	0.5498	0.2288	0.0038
	$F^{\circledast}$	1.7305	1.3335	1.1146	0.9983
$Re^{\circledast} = 1.5$	$W^{\circledast}$	1.1719	0.6655	0.2831	0.0049
	$F^{\circledast}$	1.7670	1.3449	1.1138	0.9994
$Re^{\circledast} = 2$	$W^{\circledast}$	1.3391	0.7742	0.3334	0.0059
	$F^{\circledast}$	1.8011	1.3552	1.1126	0.9987

Table 3: Longitudinal roughness $W^{\circledast}$ and $F^{\circledast}$ for condition(C_3) at different values of $Re^{\circledast}$ and w.

	w	0.4	0.6	0.8	1
$Re^{\circledast} = 0.5$	$W^{\circledast}$	0.8901	0.4775	0.1918	0.0000
	$F^{\circledast}$	1.7104	1.3256	1.1147	1.0000
$Re^{\circledast} = 1$	$W^{\circledast}$	1.0774	0.6032	0.2250	0.0000
	$F^{\circledast}$	1.7498	1.3383	1.1142	1.0000
$Re^{\circledast} = 1.5$	$W^{\circledast}$	1.2586	0.7245	0.3098	0.0000
	$F^{\circledast}$	1.7876	1.3504	1.1138	1.0000
$Re^{\circledast} = 2$	$W^{\circledast}$	1.4333	0.8408	0.3648	0.0000
	$F^{\circledast}$	1.8237	1.3615	1.1128	1.0000

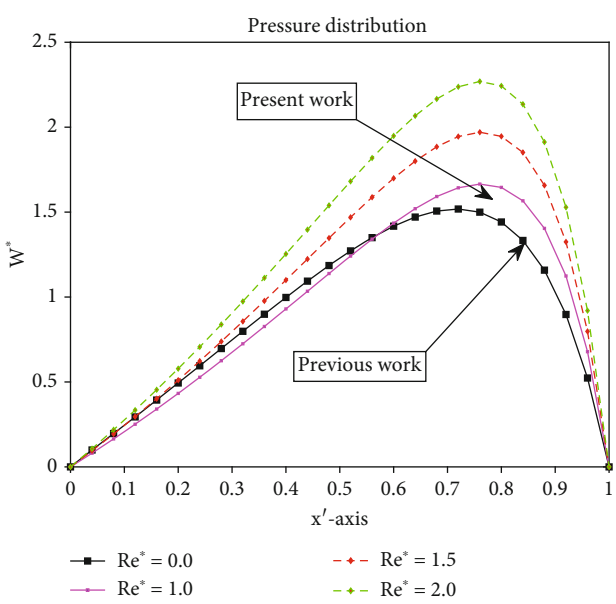

Figure 6: Pressure distributions at $T^i = T^p = T^s = 1.0$, $w = 0.4$ and for different value of $Re^{\circledast}$ (longitudinal roughness).

In this study, our work gives special attention for the following condition:

Condition (C_1): surface roughness and thermal combined effect

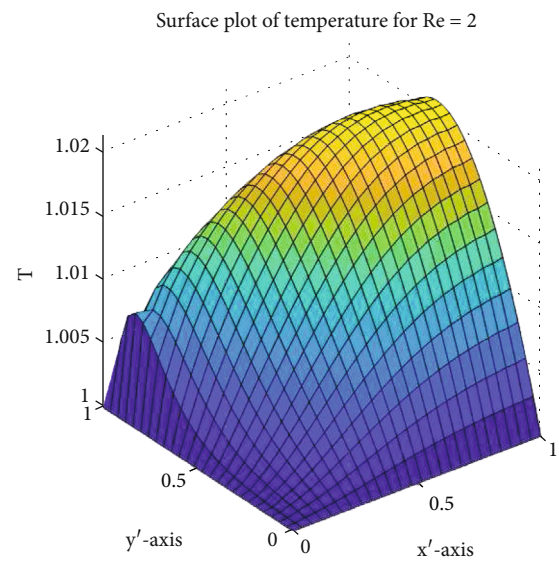

Figure 7: Temperature surface plot, combined condition C_1 at $w = 0.4$ and $T^i = T^p = T^s = 1.0$.

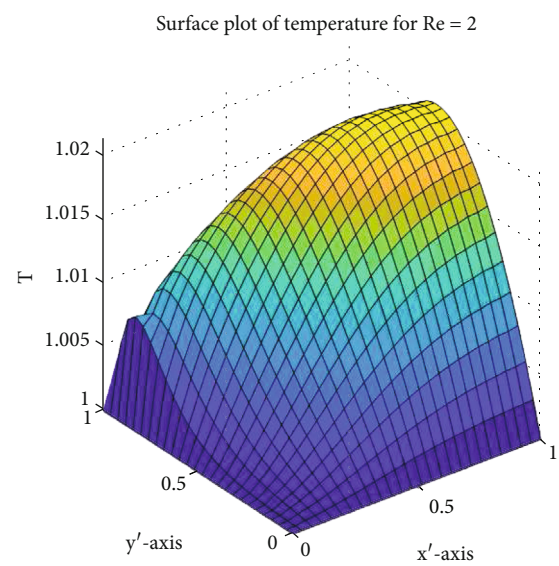

Figure 8: Temperature surface plot, thermal condition C_2 at $w = 0.4$ and $T^i = T^p = T^s = 1.0$.

Condition (C_2): thermal effect only

Condition (C_3): effect of surface roughness only

4.1. Longitudinal One-Dimensional Surface Roughness. Figure 4 illustrates the one-dimensional longitudinal distribution of pressure performance caused by the above conditions (C_1, C_2, and C_3) for various modified Reynolds numbers, considering unsteady fluid flow lubricant. For all conditions, the load-carrying capacity performance (LCCP) is in the sequence of conditions (C_1) < conditions (C_2) < conditions (C_3) at time $t = 0.01$ for each fixed value of $x^{\dagger}$. One can deduce from this that the bearing's LCCP increased as the inertial term effect $Re^{\circledast}$ increased for $t = 0.01$ constant time. Thus, increasing the inertial term effect value obstructs the

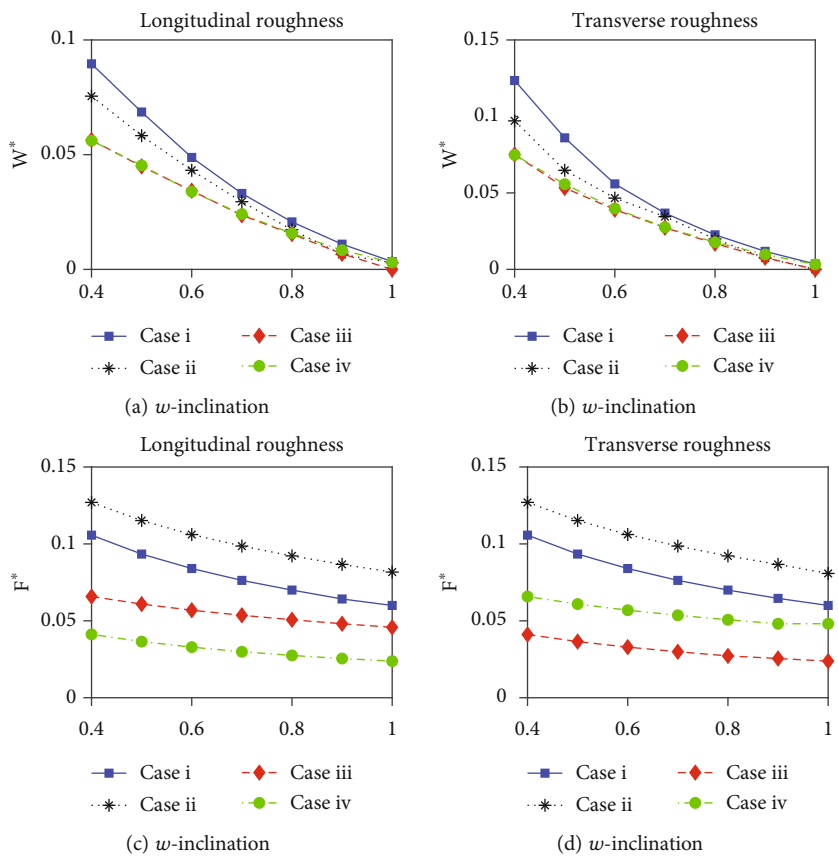

Figure 9: LCCP and friction forces for different cases.

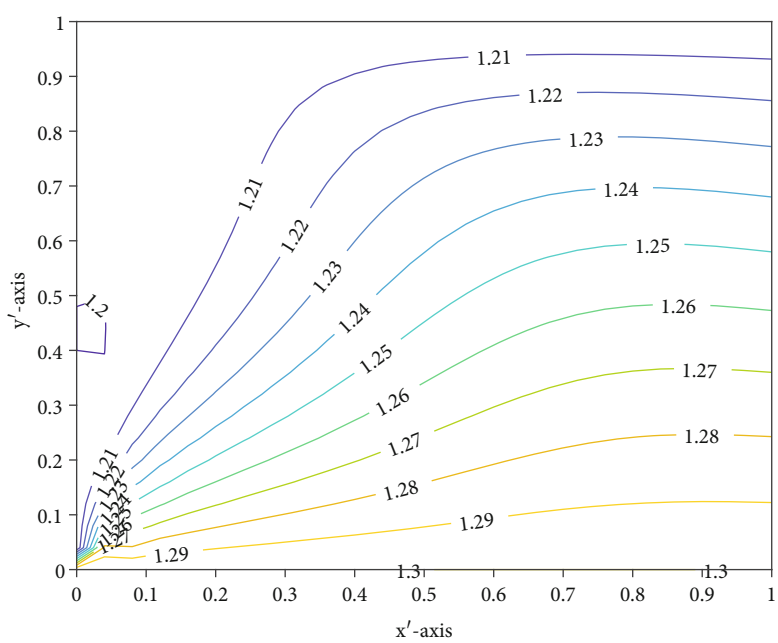

Figure 10: Temperature contour plot line for Case 1 at $w = 0.4$.

fluid flow and increases pressure. Surface roughness, on the other hand, has a greater effect than the combined and thermal effects. This demonstrates the importance of taking into account inertial terms and surface roughness effects when calculating the LCCP of plane slider bearings. In addition, the maximum curve point of the pressure is noticed closer to the

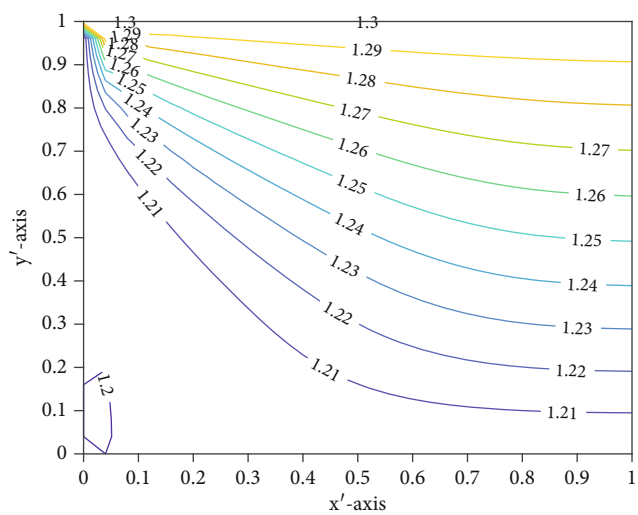

Figure 11: Temperature contour plot line for Case 2 at $w = 0.4$.

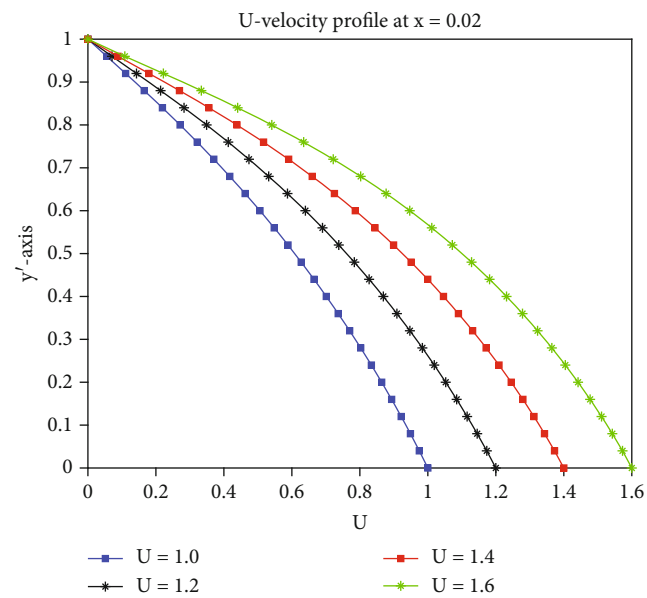

Figure 12: U-velocity profile for C_1 at $w = 0.4$ and $Re^{\circledast} = 1.0$.

Table 4: Effect of surface roughness on LCCP for different values of $\sigma^{\circledast}$, at $w = 0.4$, $\lambda^{\circledast} = 0.4$, $Re^{\circledast} = 1.0$, and $\beta^{\circledast} = 10$.

$\sigma^{\circledast}$	0.0	0.02	0.04	0.06	0.08	0.10
$w^{\circledast}$	1.0062	1.0041	0.9979	0.9877	0.9741	0.9205

Table 5: Effect of U-velocity on bearing performance for C_1 at $w = 0.4$ and $Re^{\circledast} = 1.0$.

U	1.0	1.2	1.4	1.6
$w^{\circledast}$	0.9475	0.9723	0.9925	1.0087
$F^{\circledast}$	1.7422	1.7489	1.7549	1.7588

Table 6: Performance of bearing for C_1 at $w = 0.4$ and $Re^{\circledast} = 1.0$ for different time discretization.

Δt	0.0125	0.0111	0.0100	0.0091
$w^{\circledast}$	0.9062	0.9278	0.9475	0.9679
$F^{\circledast}$	1.7315	1.7369	1.7422	1.7425

outlet, and the pattern of the graph of pressure distribution on the plane slider bearing is in good agreement with Sinha and Adamu [18], Kumar [4], Rathish Kumar and Srinivasa Rao [5] Desu Tessema et al. [22], and Naduvinamani and Angadi [24].

Figure 5 depicts the pressure distribution of the longitudinal model type for different modified Reynolds numbers due to the fluid inertial term effect at $w = 0.4$, of temperature $T^i = T^p = T^s = 1.0$, and condition (C_1). From this, one can observe that as the modified Reynolds number increases, the LCCP of the plane slider bearing increases. Furthermore, again from Tables 1–3, as the modified Reynolds number increases, the corresponding drag force increases. This result is in good agreement with Malvano and Vatta [16] and Sestieri and Piva [12].

At an inclination of $w = 0.4$, $T^i = T^p = T^s = 1.0$, and for surface roughness and thermal combined effect, Figure 6 displays the pressure distribution for an unsteady fluid flow lubricant of a plane slider bearing for various modified Reynolds numbers. This suggests that the current study is superior to earlier work when compared to the steady laminar flow of the pressure distribution, which is carried out in Sinha and Adamu [18] and Desu Tessema et al. [22]. In comparison to other methods that are described in the literature, our method generally has a better LCCP.

The LCCP and drag force of one-dimensional longitudinal roughness for various inertial term effect values corresponding to the stated conditions are displayed in Tables 1–3. We see an almost 5% improvement in load-carrying capacity performance between condition (C_1) and condition (C_2) in all inertial term effect values at $w = 0.4$. Similarly, Tables 1 and 2 demonstrate that there is a drag force of less than 1% at $w = 0.4$.

Furthermore, we observed a 13% decrement in LCCP and a negligible change in drag force for all $Re^{\circledast}$ values between condition (C_3) and condition (C_1) at $w = 0.4$ in Tables 1 and 3. This happens because the density and viscosity of the lubricant's fluid are reduced because of the condition (C_1) effect. As a result, the LCCP is reduced. Even if the LCCP of a parallel slider bearing at $w = 1$ is small, a better LCCP is generated with condition (C_1) and condition (C_2) in comparison to condition (C_3) due to fluid expansion as the lubricant temperature rises.

A one-dimensional longitudinal surface roughness model assumes that the texture has the appearance of furrows, long narrow ridges, and valleys in the sliding direction (x-axis), allowing for fast lubricant flow and resulting in a decrease in pressure distribution, implying a reduction in load-carrying capacity (LCC).

Figures 7 and 8 show the surface plot of temperature for one-dimensional longitudinal surface roughness in the cases

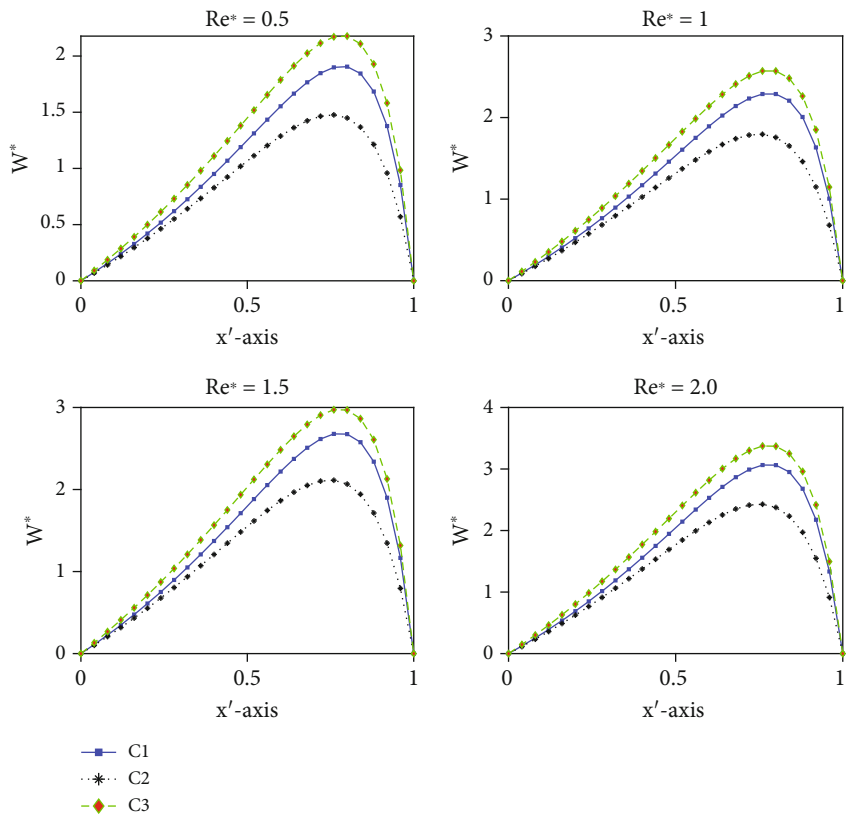

Figure 13: Pressure distributions at $T^i = T^p = T^s = 1.0$ and $w = 0.4$ for different value of $\mathrm{Re}^{\circledast}$ (transversal roughness).

of conditions C_1 and C_2 at $\mathrm{Re}^{\circledast} = 2$. Both surface plots of temperature graphs show that there is no significant variation in temperature values.

In parallel plane slider bearings, if the temperature of surface of the pad bearing is higher than the slider temperature of surface, a suction action may occur, according to Zienkiewicz [35]. The study of the surface thermal impact on the plane slider and pad at a certain temperature of ($T^s < T^p$ or $T^s > T^p$) on the LCC and frictional force of a plane slider bearing is of excessively realistic relevance. In practice, the fixed surface is typically warmer than the moving surface, according to Pinkus and Sternlicht [36]. Another critical scenario in a slider bearing application is that the inlet lubricant temperature is lower than the slider and pad temperatures. Based on this, the combined thermal and surface roughness effects (C_1) of the following temperature boundary conditions have been investigated with a modified Reynolds number $\mathrm{Re}^{\circledast} = 0.05$:

Case 1. $T^i = T^p = 1.2$ and $T^s = 1.3$.

Case 2. $T^i = T^s = 1.2$ and $T^p = 1.3$.

Case 3. $T^i = 1.2$, $T^s = 1.3$, and $T^p = 1.4$.

Case 4. $T^s = 1.4$, $T^i = 1.2$, and $T^p = 1.3$.

Drag forces and LCCP for one-dimensional longitudinal and transverse surface roughness are shown in Figure 9 at $\mathrm{Re}^{\circledast} = 0.05$ of inertial term effect. The inlet temperature is equal to or less than the temperatures of the slider (movable) and pad (stationary) of plane slider bearing.

When the temperature of the pad (stationary) and slider (movable) is different, there is an 18% difference in loading performance between Case 2 and Case 1 for $w = 0.4$ as shown in Figure 9(a). For $w = 1$, Case 1's LCCP is slightly better than Case2's. In the case of drag force, there is a significant difference between Case 2 and Case 1 as we observe from Figure 9(c).

These figures show that if the inlet temperature is lower than that of the pad and slider of plane slider bearing, Case 4's drag force of friction and LCCP are lower than Case 3's for each inclination parameter. According to these various factors, if the slider temperature is higher than the pad temperature, the temperature may drop due to the inertial term effect, increasing the LCCP and drag friction force.

For a better understanding, the temperature surface contour plots of Case 1 and Case 2 for $w = 0.4$ are shown in Figures 10 and 11. Case 2's load-carrying capacity is lower than Case 1's because Case 2 has total higher average temperature than Case 1.

The performance of LCCP for different ($\delta^{\circledast}$) values is shown in Table 4 at a modified inertial value of $\mathrm{Re}^{\circledast} = 1.0$. We can see from this table that as $\delta^{\circledast}$ increases, the bearing's LCCP decreases. This is because the surface roughness

Table 7: Transversal roughness $W^{\circledast}$ and $F^{\circledast}$ for condition(C_1) at various value of $Re^{\circledast}$ and w.

	w	0.4	0.6	0.8	1
$Re^{\circledast} = 0.5$	$W^{\circledast}$	1.0507	0.4916	0.1897	0.0027
	$F^{\circledast}$	1.7722	1.3278	1.1150	1.0000
$Re^{\circledast} = 1$	$W^{\circledast}$	1.2746	0.6283	0.2525	0.0040
	$F^{\circledast}$	1.7858	1.3420	1.1145	0.9997
$Re^{\circledast} = 1.5$	$W^{\circledast}$	1.4917	0.7592	0.3120	0.0052
	$F^{\circledast}$	1.8309	1.3551	1.1136	0.9993
$Re^{\circledast} = 2$	$W^{\circledast}$	1.7009	0.8832	0.3672	0.0062
	$F^{\circledast}$	1.8735	1.3669	1.1123	0.9986

(asperity) increases, allowing for faster lubricant flow and a decrease in pressure distribution for the one-dimensional longitudinal roughness model; however, it is the converse for the one-dimensional transversal roughness model.

4.2. U-Velocity Profile. Plotting of a one-dimensional longitudinal roughness U-velocity profile with different boundary condition U values of the slider for condition (C_1) at $x = 0.02$ is shown in Figure 12. This indicates that the full U-velocity increases as the slider's U value increases.

Table 5 displays the influence of U-velocity for condition (C_1). It is evident that raising the U value enhances the ability to withstand load and drag forces. This is because, in addition to the effects of inertial forces and surface roughness, an increasing U value accelerates the fluid in the sliding direction. The fluid's viscosity increases with even a small increase in temperature, which enhances the bearing capacity.

Table 6 shows the bearing performance for the combined effect (C_1) at different time discretization. As anyone can observe from the table, as time discretization increases, unsteady fluid flow lubricant bearing performance rises also.

4.3. One-Dimensional Transverse Roughness. With unsteady fluid flow taken into consideration, Figure 13 shows a one-dimensional unsteady fluid flow lubricant transverse roughness distribution of pressure performance produced by the aforementioned conditions (C_1, C_2, and C_3) for different inertial values. At a time discretization of $t = 0.01$, the LCCP is in the sequence of conditions (C_2) < conditions (C_1) < conditions (C_3) for each fixed value of $x^{\dagger}$. This indicates that the LCCP of the bearing grew at $t = 0.01$ constant time as the fluid inertial term's influence increased. Consequently, increasing the inertial fluid effect causes pressure to rise and obstructs fluid movement. Moreover, under all circumstances, surface roughness has a bigger impact than both combined and thermal impacts.

Regarding the time-dependent pressure equation's slider and pad at different temperatures. For a fixed modified Reynolds number value of $Re^{\circledast} = 0.5$, the distribution of pressure in Figure 9(b) has a slightly higher LCCP than the one-dimensional longitudinal distribution but otherwise follows the same pecking order. The drag force results for one-dimensional longitudinal roughness in Cases 1–4 are almost the same as those for one-dimensional transverse roughness,

Table 8: Transversal roughness $W^{\circledast}$ and $F^{\circledast}$ for condition(C_2) at various value of $Re^{\circledast}$ and w.

	w	0.4	0.6	0.8	1
$Re^{\circledast} = 0.5$	$W^{\circledast}$	0.8460	0.4282	0.1707	0.0025
	$F^{\circledast}$	1.7071	1.3224	1.1151	1.0000
$Re^{\circledast} = 1$	$W^{\circledast}$	1.0356	0.5580	0.2281	0.0038
	$F^{\circledast}$	1.7486	1.3353	1.1147	0.9988
$Re^{\circledast} = 1.5$	$W^{\circledast}$	1.2184	0.6665	0.2824	0.0049
	$F^{\circledast}$	1.7883	1.3473	1.1140	0.9994
$Re^{\circledast} = 2$	$W^{\circledast}$	1.3937	0.7765	0.3328	0.0058
	$F^{\circledast}$	1.8258	1.3581	1.1129	0.9987

Table 9: Transversal roughness $W^{\circledast}$ and $F^{\circledast}$ for condition(C_3) at various value of $Re^{\circledast}$ and w.

	w	0.4	0.6	0.8	1
$Re^{\circledast} = 0.5$	$W^{\circledast}$	1.2133	0.5705	0.2193	0.0000
	$F^{\circledast}$	1.7703	1.3349	1.1143	1.0000
$Re^{\circledast} = 1$	$W^{\circledast}$	1.4483	0.7154	0.2865	0.0000
	$F^{\circledast}$	1.8192	1.3496	1.1140	1.0000
$Re^{\circledast} = 1.5$	$W^{\circledast}$	1.6784	0.8561	0.3512	0.0000
	$F^{\circledast}$	1.8665	1.3635	1.1133	1.0000
$Re^{\circledast} = 2$	$W^{\circledast}$	1.9027	0.9917	0.4128	0.0000
	$F^{\circledast}$	1.9119	1.3764	1.1124	1.0000

as shown in Figure 9(d). With that exception, Cases 4 and 3 are reversed.

The LCCP and drag force for unsteady fluid flow lubricant of one-dimensional transverse roughness for different fluid inertial terms corresponding to the aforementioned conditions are shown in Tables 7–9. At an inclination of $w = 0.4$, there is a nearly 19% difference in LCCP between condition (C_1) and condition (C_2). Similarly, at $w = 0.4$, there is a 2% difference in drag force for all modified Reynolds numbers at $Re^{\circledast}$.

Moreover, for all $Re^{\circledast}$ values between condition (C_3) and condition (C_1) at $w = 0.4$, we observed a nearly 13% difference in LCCP and a 2% difference in drag force, as shown in Tables 7 and 9. Because of the combined effect, the density and viscosity of the lubricant's fluid are reduced. The LCCP is reduced as a result. Tables 8 and 9 demonstrate that for $w = 0.4$, there is a significant difference in LCCP between condition (C_3) and condition (C_2). There is also a 26% difference in value for transverse frictional force over all modified Reynolds number values between condition (C_3) and condition (C_2). Even if a parallel slider bearing's LCCP is small at $w = 1$, there is an LCCP generated in condition (C_1) and condition (C_2) in comparison to condition (C_3) due to fluid expansion as the lubricant temperature rises.

Due to the plane slider bearing nature of our consideration, when there is transverse roughness for unsteady fluid flow lubricant, the fluid typically only travels in the x-direction and must pass through a series of constrictions at the flow

gap, or fluid film domain area. In addition to the inertial term effect, this will impede the flow. The widening due to valleys of surface asperities, on the other hand, will ease the flow.

5. Conclusion

In this work, time-dependent fluid flow pressure and momentum equation in slider bearings were evaluated via FEM to analyze the bearing characteristics (LCCP and drag force) of the one-dimensional longitudinal and transverse models. In both types of models for nonparallel slider bearings, the achievement of the bearing characteristics improves. However, for $w = 1$ (parallel), the performance of the bearing is negligible. Furthermore, in the case of condition (C_1) taking the thermal of the slanted pad slider as higher than the thermal of the pad, in both models, LCCP rises for nonparallel bearing, whereas it goes to zero for parallel ($w = 1$). The opposite is true for drag force in both model types. As the modified Reynolds number increases, the inertial terms become increasingly important, and the geometrical configuration of the film differs significantly from that obtained using the elementary lubrication theory. This is due to fluid inertial term effects from unsteady fluid flow in addition to the surface roughness effect. This demonstrates the significance of taking surface texture and inertial effects into account due to unsteady fluid flow lubricant. One-dimensional transversal models typically have a pressure distribution that is larger than that of one-dimensional longitudinal slider bearings in the situation of unsteady fluid flow lubrication.

A superscript "⊛" indicates the nondimensional quantity.

Symbols

δ: Random distribution of roughness
μ: Viscosity of the lubricant
μ_{av}: Average viscosity across the film
ρ: Density of the lubricant
ρ_{av}: Average density across the film
σ^2: Variation of roughness
B: Bearing width
E: Expected value operator
E_c: Eckert number
h: Nominal film thickness
h_0: Nominal film thickness at outlet
h_i: Nominal film thickness at inlet
H_t: Height of rough surface
k: Thermal conductivity of lubricant
P: Lubricant pressure
p_e: Peclet number
p_i: Inlet pressure
p_r: Prandtl number
T: Lubricant temperature
T_{av}: Average temperature across the film
U: Velocity of the moving surface
v: Velocity in the direction of the y-coordinate
w: h_0/h_i
$W^{\circledast}$: Load-carrying capacity of the bearing
$x^\dagger, y^\dagger$: Transformed coordinate system.

Data Availability

There is no data that has been used for this research.

Conflicts of Interest

The authors declare that they have no conflicts of interest.

References

[1] J.-R. Lin, "Surface roughness effect on the dynamic stiffness and damping characteristics of compensated hydrostatic thrust bearings," *International Journal of Machine Tools and Manufacture*, vol. 40, no. 11, pp. 1671–1689, 2000.

[2] S. Guha, "Analysis of steady-state characteristics of misaligned hydrodynamic journal bearings with isotropic roughness effect," *Tribology International*, vol. 33, no. 1, pp. 1–12, 2000.

[3] H. Christensen and K. Tonder, "The hydrodynamic lubrication of rough bearing surfaces of finite width," *Journal of Lubrication Technology*, vol. 93, no. 3, pp. 324–329, 1971.

[4] B. R. Kumar, "A segregated SUPG/FEM for THDL analysis in high speed slider bearings with injection effect," *Journal of Tribology*, vol. 123, no. 4, pp. 732–741, 2001.

[5] B. Rathish Kumar and P. Srinivasa Rao, "Streamline upwind Pertov-Galerkin finite element analysis of thermal effects on load carrying capacity in slider bearings," *Numerical Heat Transfer Part A-Applications*, vol. 38, no. 3, pp. 305–328, 2000.

[6] P. Andharia, J. Gupta, and G. Deheri, "Effect of surface roughness on hydrodynamic lubrication of slider bearings," *Tribology Transactions*, vol. 44, no. 2, pp. 291–297, 2001.

[7] S. F. Alyaqout and A. A. Elsharkawy, "Optimum shape design for surface of a thermohydrodynamic lubrication slider bearing," *Lubrication Science*, vol. 25, no. 6, pp. 379–395, 2013.

[8] P. Thakkar, H. Patel, and G. Deheri, "Transeversely rough narrow width tapered pad bearing," *Indian Journal of Science and Technology*, vol. 10, no. 9, pp. 1–6, 2017.

[9] M. Chawla and R. Bhardwaj, "Surface roughness effect on couple stress fluid lubricated porous pivoted slider bearings," *Journal of Information and Optimization Sciences*, vol. 37, no. 1, pp. 13–22, 2016.

[10] A.-G. M. Rahman, "Effects of variable viscosity and thermal conductivity on unsteady MHD flow of non-Newtonian fluid over a stretching porous sheet," *Thermal Science*, vol. 17, no. 4, pp. 1035–1047, 2013.

[11] A. Ali, S. Saba, S. Asghar, and S. Saleem, "Thermal and concentration effects of unsteady flow of non-Newtonian fluid over an oscillating plate," *Comptes rendus de l'Académie bulgare des Sciences*, vol. 71, no. 4, 2018.

[12] A. Sestieri and R. Piva, "The influence of fluid inertia in unsteady lubrication films," *Journal of Lubrication Technology*, vol. 104, no. 2, pp. 180–186, 1982.

[13] N. Abbas, S. Nadeem, and M. Khan, "Numerical analysis of unsteady magnetized micropolar fluid flow over a curved surface," *Journal of Thermal Analysis and Calorimetry*, vol. 147, no. 11, pp. 6449–6459, 2022.

[14] I. Syed and M. Sarangi, "Hydrodynamic lubrication with deterministic micro textures considering fluid inertia effect," *Tribology International*, vol. 69, pp. 30–38, 2014.

[15] T. Ota, H. Yoshikawa, M. Hamasuna, T. Motohashi, and S. Oi, "Inertia effects on film rupture in hydrodynamic lubrication," *Journal of Tribology*, vol. 117, no. 4, pp. 685–690, 1995.

[16] R. Malvano and F. Vatta, "The influence of fluid inertia in steady laminar lubrication," *Journal of Lubrication Technology*, vol. 105, no. 1, pp. 77–83, 1983.

[17] D. Prasad, P. Singh, and P. Sinha, "Thermal and inertia effects in hydrodynamic lubrication of rollers by a power law fluid considering cavitation," *Journal of Tribology*, vol. 115, no. 2, pp. 319–326, 1993.

[18] P. Sinha and G. Adamu, "THD analysis for slider bearing with roughness: special reference to load generation in parallel sliders," *Acta Mechanica*, vol. 207, no. 1-2, pp. 11–27, 2009.

[19] G. Adamu and P. Sinha, "Thermal and roughness effects in a tilted pad slider bearing considering heat conduction through the pad and slider," *Proceedings of the National Academy of Sciences, India Section A: Physical Sciences*, vol. 82, no. 4, pp. 323–333, 2012.

[20] D. Singh, N. Singh, and R. Awasthi, "Effect of surface texture parameters on the performance of finite slider bearing," *Materials Today: Proceedings*, vol. 5, no. 9, pp. 19349–19358, 2018.

[21] G. Alexander Raymand and I. Jayakaran Amalraj, "Inertia effects in rheodynamic lubrication of an externally pressurized converging thrust bearing using Bingham fluids," *Journal of Applied Fluid Mechanics*, vol. 12, no. 2, pp. 587–594, 2019.

[22] G. Desu Tessema, G. Adamu Derese, and A. Andargie Tiruneh, "Thermal and surface roughness effects on performance analysis of slider bearing via Petrov–Galerkin finite element method," *Mathematical Problems in Engineering*, vol. 2022, Article ID 4216136, 18 pages, 2022.

[23] G. D. Tessema, G. A. Derese, and A. A. Tiruneh, "Analysis of thermal and surface roughness effects of slider bearing in the case of turbulent lubricant flow using finite element method," *Research in Mathematics*, vol. 10, no. 1, article 2250492, 2023.

[24] N. Naduvinamani and A. Angadi, "Static and dynamic characteristics of rough porous Rayleigh step bearing lubricated with couple stress fluid," *Lubricants*, vol. 10, no. 10, p. 257, 2022.

[25] N. B. Naduvinamani and A. Angadi, "On the dynamic characteristics of rough porous inclined slider bearing lubricated with micropolar fluid," *Tribology Online*, vol. 17, no. 1, pp. 59–70, 2022.

[26] Y. Gu, J. Cheng, C. Xie, L. Li, and C. Zheng, "Theoretical and numerical investigations on static characteristics of aerostatic porous journal bearings," *Machines*, vol. 10, no. 3, p. 171, 2022.

[27] C. Fang, A. Zhu, W. Zhou, Y. Peng, and X. Meng, "On the stiffness and damping characteristics of line contacts under transient elastohydrodynamic lubrication," *Lubricants*, vol. 10, no. 4, p. 73, 2022.

[28] W. Jamshed, A. K. Alanazi, S. S. P. M. Isa et al., "Thermal efficiency enhancement of solar aircraft by utilizing unsteady hybrid nanofluid: a single-phase optimized entropy analysis," *Sustainable Energy Technologies and Assessments*, vol. 52, article 101898, 2022.

[29] M. Raees, M. Hussain, N. Bibi et al., "Energy transport analysis of the magnetized forced flow of power-law nanofluid over a horizontal wall," *Journal of Magnetism and Magnetic Materials*, vol. 560, article 169681, 2022.

[30] C. Hooke, "Fluid film lubrication: theory and design, Andras Z. Szeri, Cambridge University Press, Cambridge, 1998, 414 pp., ISBN 0521 48100 7, £55.00," *Tribology International*, vol. 32, no. 6, pp. 345–347, 1999.

[31] H. Christensen and K. Tonder, "Tribology of rough surfaces: stochastic models of hydrodynamic lubrication," *Sintef Report*, vol. 10, no. 69, p. 18, 1969.

[32] H. Christensen, "Stochastic models for hydrodynamic lubrication of rough surfaces," *Proceedings of the Institution of Mechanical Engineers*, vol. 184, no. 1, pp. 1013–1026, 1969.

[33] A. N. Brooks and T. J. Hughes, "Streamline upwind/Petrov-Galerkin formulations for convection dominated flows with particular emphasis on the incompressible Navier-Stokes equations," *Computer Methods in Applied Mechanics and Engineering*, vol. 32, no. 1-3, pp. 199–259, 1982.

[34] M. Schumack, "Application of the pseudospectral method to thermohydrodynamic lubrication," *International Journal for Numerical Methods in Fluids*, vol. 23, no. 11, pp. 1145–1161, 1996.

[35] O. Zienkiewicz, "Temperature distribution within lubricating films between parallel bearing surfaces and its effect on the pressures developed," *Proceedings of the Conference on Lubrication and Wear*, vol. 135, 1957.

[36] O. Pinkus and B. Sternlicht, *Theory of Hydrodynamic Lubrification*, McGraw-Hill, 1961.